Spring 2020

# Shock wave propagation behavior at corners and crosscuts in five small-scale tunnel scenarios

David Pierre Doucet



Department:

# SHOCK WAVE PROPAGATION BEHAVIOR AT CORNERS AND CROSSCUTS IN FIVE SMALL-SCALE TUNNEL SCENARIOS

by

DAVID PIERRE DOUCET

A THESIS

Presented to the Faculty of the Graduate School of the

MISSOURI UNIVERSITY OF SCIENCE AND TECHNOLOGY

In Partial Fulfillment of the Requirements for the Degree

MASTER OF SCIENCE IN EXPLOSIVES ENGINEERING

2020

Approved by:

Dr. Catherine E. Johnson, Advisor
Dr. Kyle Perry
Dr. Paul Worsey

# ABSTRACT

Shock wave propagation in tunnels and other enclosed environments is substantially more complicated than in an open-air or even a surface detonation. There is still much to learn about how shock wave properties change as a wave propagates in an enclosed space, such as a mine tunnel, inside of a building, or city street. The geometry of the enclosure will have a large role in the propagation of the shock wave. This means that many different tunnel designs must be studied. This work tested five different designs using a modular small-scale model. The scenarios tested were Straight-line, Single Turn, Around Pillar, Split, and Split Around Pillar. Piezoelectric pressure transducers were used to determine peak pressure and maximum impulse at designated locations in the model. The results of this research show where high- and low-pressure zones are formed during an explosion based on the corner and crosscut features of the tunnel. Some key findings from these experiments include the minimal pressure change observed through the crosscut in the Single Turn arrangement and the significant pressure drop downstream of the pillar in the Around Pillar scenario. The data analysis also proved that pressure experienced at the exit is more greatly affected by the geometry of the tunnel than the tunnel's total volume. This information will help improve mine planning concerning the location of both personnel and equipment so that they will be less likely to be injured or damaged in the event of an accidental explosion. The information will also lead to safer procedures for explosive breaching personnel and a larger base of knowledge for investigating and mitigating urban bombings.

# ACKNOWLEDGMENTS

I would like to thank everyone who has been a part of this project for helping me complete this thesis and earn my master's degree in Explosives Engineering. I want to start by acknowledging Dr. Catherine Johnson for her guidance as my advisor through my graduate schooling. She is a great leader for the Energetics Research Team, and I would not have been able to complete this thesis without her support and expertise.

Next, I need to thank Joe Schott, Chance Moore, Jeffrey Heniff, and Fred Eickelmann for their help in building the scale model and conducting the testing for this thesis. Without their assistance I might still be trying to get the model put together behind the Rock Mechanics and Explosives Research Center (RMERC) building.

I also want to thank Dr. Barbara Rutter and my fellow graduate students, Marty Langenderfer and Kelly Williams for proofreading this thesis and helping to bring it to a level of writing worthy of this degree.

Thank you to the members of my advisory committee, Dr. Kyle Perry and Dr. Paul Worsey, for the time you took to teach me throughout my years at Missouri S&T and for your input with this thesis project.

Lastly, I would like to thank my family for their unwavering support through my entire education journey. Their love, patience, and faith has given me the resolve to pursue my higher education goals and to reach this achievement.

# TABLE OF CONTENTS

Page

# LIST OF FIGURES

Page

# LIST OF TABLES

Page

# NOMENCLATURE

| Abbreviation | Full Name |
|---|---|
| µs | Microsecond |
| ANFO | Ammonium Nitrate Fuel Oil |
| bTBI | Blast Induced Traumatic Brain Injury |
| DAS | Data Acquisition System |
| DDT | Deflagration to Detonation Transition |
| fps | Frames per Second |
| ft | Foot or Feet |
| g | Gram |
| Hz | Hertz or Samples per Second |
| IED | Improvised Explosive Device |
| IMESAFR | Institute of Makers of Explosives Safety Analysis for Risk |
| in | Inch / Inches |
| kg | Kilogram |
| lbs | Pounds |
| mg | Milligram |
| Missouri S&T | Missouri University of Science and Technology |
| ms | Millisecond |
| P | Pressure |

| | |
|---|---|
| PETN | Pentaerythritol Tetranitrate |
| $P_i$ | Pressure value at current time step |
| $P_{i+1}$ | Pressure value at next time step |
| $P_s$ | Peak Pressure |
| psi | Pound Force per Square Inch |
| psi*ms | Unit of Impulse (Pound Force per Square Inch multiplied by Milliseconds) |
| R | Distance to Charge |
| $R_1$ | Full Scale Distance to Charge |
| $R_2$ | Small Scale Distance to Charge |
| RDX | Royal Demolition Explosive or Cyclotrimethylenetrinitramine |
| RMERC | Rock Mechanics and Energetics Research Center |
| SD | Scaled Distance |
| t | Time |
| $t^+$ | Positive Phase Duration |
| TATP | Triacetone Triperoxide |
| $t_i$ | Time value at current time step |
| $t_{i+1}$ | Time value at next time step |
| W | Charge Weight |
| $W_1$ | Full Scale Charge Weight |
| $W_2$ | Small Scale Charge Weight |

# 1. INTRODUCTION

## 1.1. PROBLEM STATEMENT

Shock wave propagation in tunnels and other enclosed environments is substantially more complicated than in an open-air or even a surface detonation. With many reflective surfaces and greater confinement, predicting blast characteristics in these environments can be difficult. While these situations are more difficult to analyze, many energetic events occur in an enclosed space. It is important to continue to study blast wave propagation in these environments so the propagation phenomena can be understood more fully, and this greater understanding can be put to proper use. To gain this better understanding, a small-scale model has been designed and fabricated. This model has modular capabilities that allow for testing of different tunnel pathways and corridor designs. In this work, five different tunnel designs have been tested, and the data analysis will be used to test the following hypotheses:

- Pressure dead zones and concentration points can be identified and correlated to tunnel features.
- Any effect total tunnel volume has on the blast characteristics at the tunnel exit is outweighed by the effects from the shape of the pathway.

## 1.2. RESEARCH APPLICATIONS

Coal mines, developed urban areas, and building interiors, are three confided spaces where explosions occur. Dust explosions are historically one of the leading causes of disasters in coal mines, terrorist bombings are more frequently occurring in cities around

the world, and military and police personnel utilizing explosive breaching techniques are periodically exposed to blast overpressure throughout their careers. In each of these scenarios, the confined space exacerbates the damage done by the explosion, and a better understanding of blast wave characteristics in confined spaces could help mitigate damage in the future.

**1.2.1. Mine Safety.** Mining plays a major role in the United States and global economies. From coal mines that provide the energy source for electrical powerplants to metal/nonmetal mines, which provide the elements needed to manufacture the devices that require the electricity, mining touches many aspects of everyday life. Mining has varying hazards based on the material being mined, and the extraction methods being employed. Underground coal mines are one of the most dangerous work environments, and "The most significant and powerful hazard that exists in an underground coal mine is a coal dust explosion" [1]. Improved understanding of shock propagation in a tunnel environment can help mine engineers design mine plans that are less likely to amplify the blast pressures, and to place equipment and personnel where they will be best shielded from an accidental explosion.

**1.2.2. Urban Bombings.** With the increase in global terrorism over the past few decades, improvised explosive devices (IEDs) are being used in populated urban environments where the device will do the most damage and cause the highest casualties. Some examples of these attacks are the 1993 World Trade Center Bombing, the 1995 Oklahoma City Bombing, and the 2019 Sri Lanka Easter Bombings [2, 3, 4]. Each of these attacks were committed in urban areas with explosives either in a vehicle or on someone's person. When an explosive is detonated in an urban setting with high building density and

tall structures, the buildings act to confine the explosion. The shock from the explosion will reflect off building surfaces and be focused down city streets, amplifying the damage at certain locations. The study of shock wave behavior in these kinds of confined spaces can help predict damage from future attacks, or improve post blast forensic analysis, helping investigators more quickly and accurately determine where a blast originated. More information on shock wave propagation in confined spaces can also be used to improve blast resistant designs for buildings and other public spaces.

**1.2.3. Explosive Breaching.** In both military and law enforcement roles, there are situations where soldiers or officers need to enter a building or room and the use of force is required to gain entry. In many cases the fastest and safest way to create access is through explosive breaching, where explosive charges are used to either break open a door or break through a wall. Over a career, breaching personnel will be exposed repeatedly to air blast overpressure produced by the breaching charge, and this repeated blast exposure may lead to mild traumatic brain injury or other cognitive issues [5]. A better understanding of shock wave propagation in hallways and interior spaces can be applied to breacher training and protocol so that soldiers and officers can arrange themselves to receive the lowest possible levels of blast overpressure.

# 2. BACKGROUND

This section provides background information on the motivation for this research, specifically mine disasters, urban bombings, and explosive breaching safety. It will also introduce the reader to concepts that were utilized to develop the methodology and complete the data analysis for this research. Specifically, these topics are an explosives overview, and introduction to shock wave behavior, and a discussion on explosive scaling laws. The explosives overview will discuss key differences between high and low explosives as well as the distinctions between primary and secondary explosives. The introduction to shock wave behavior will look at the three most common scenarios utilized in the study of explosives, namely free-air, surface, and shock tunnel detonations, and discuss the behavior observed in each. Lastly, the scaling law section will show how the small-scale testing completed in this thesis can be compared to full scale scenarios.

## 2.1. EXPLOSIVES OVERVIEW

The subject of this thesis is explosive driven shock wave propagation through tunnels. An explosive is “any substance or device that can be made to produce a volume of rapidly expanding gas in a brief period” [6]. Explosives are typically categorized by their sensitivity and reaction characteristics. An explosive material can be considered a high or low explosive based on whether it detonates or deflagrates. Initiation of a low explosive causes the material to burn or deflagrate. Deflagration is defined as “combustion which propagates through a gas or across the surface of an explosive at subsonic speeds, driven by the transfer of heat” [7]. High explosives, on the other hand, typically detonate when

initiated. A detonation is defined as “combustion of a substance which is initiated suddenly and propagates extremely rapidly, giving rise to a shock wave” [8]. A detonation wave consists of a leading shock that compresses the explosive material, followed by a reaction zone where the product gasses are created and begin to expand [9]. When this detonation wave reaches the edge of the explosive, the energy from the reaction is transferred into the surrounding medium, creating a shock wave that propagates away from the explosive in all directions.

Another way to classify an explosive is by sensitivity to stimulus. The terms primary and secondary explosive are typically used to describe an energetic material’s sensitivity. Primary explosives “are extremely sensitive to mechanical shock, friction, and heat, to which they will respond by burning rapidly or detonating.” Secondary explosives “are relatively insensitive to shock, friction, and heat” [10]. Typically, the shock from a primary explosive is required to initiate detonation in a secondary explosive; this is called the “Explosive Train” [11]. When using low explosives, the explosive train usually only requires two components, the ignitor and the main charge. The ignitor would be a flame or spark creating device that will initiate a combustion reaction in the low explosive charge which will then accelerate into a deflagration. In high explosive trains, a three-component configuration is often used. This three part explosive train will utilize both a detonator and a booster to initiate the main charge, and will be used when the detonator does not release enough energy to reliably start a detonation reaction in the main charge [12]. When an explosive is so insensitive that a booster charge is almost always used it may be considered a tertiary explosive; examples of tertiary explosives are ammonium nitrate fuel oil (ANFO) and other blasting agents [10]. In this three-part train, the detonator will usually have a very

small amount of primary explosive that is used to initiate a larger amount of sensitive secondary explosive, like RDX or PETN. The booster will be made from a larger amount of secondary explosive, ranging from 10g up to 900g [13]. Lastly, the main charge will consist of a large quantity of secondary or tertiary explosive, such as ANFO or emulsion. Figure 2.1 provides an illustration of a typical explosive train.

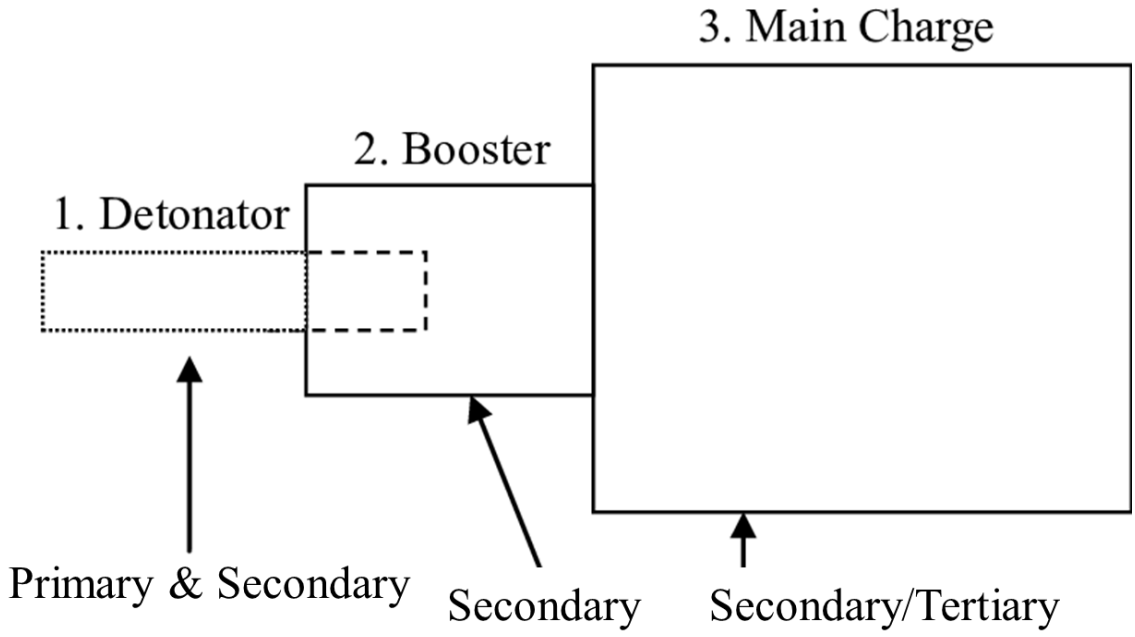


Figure 2.1: Explosive Train Diagram (Adapted from [12])

The explosives used for breaching and in urban bombings are typically high explosives because they detonate and have high brisance, which is the shattering or crushing effect from an explosion [14]. For breachers, the high brisance is needed to successfully break down the target barrier. Handling safety is also important for breachers, so they use detonating cord, composition C4, or other secondary high explosives with low

sensitivity to complete the task [15]. In urban bombings the perpetrator(s) desire greater structural damage or fragmentation from their explosive device which is also related to high brisance.

The methane/air and coal dust/air reactions seen in mine explosions can be difficult to classify with the standard terminology. With both of these fuel/air mixtures, if they are initiated in an open space with a weak energy source, such as a spark or flame, the mixture will deflagrate [16]. In this case, the mixed components are behaving like primary low explosives, initiating from a low energy stimulus and burning rapidly but not reacting at the speed of sound in the materials. However, when confined in a rough walled tube, similar to a mine entry, the deflagration can accelerate and undergo a deflagration to detonation transition (DDT). The flame acceleration needed for a deflagration to detonation transition in influenced by wall roughness, tunnel length, and fuel/air mixture [16, 17, 18]. Rough walls create more turbulence which accelerates the flame front, longer tunnels provide more time for the flame to accelerate, and a stoichiometric fuel/air ratio will undergo DDT faster than an imperfect mixture [16, 17, 18]. After this transition the mixture more closely resembles a high explosive, reacting faster than the speed of sound in the material, with little distance between the reaction front and the propagating shock wave. In a mine explosion scenario, the methane pop and initial coal dust explosion would be a low explosive deflagration. As the coal dust explosion propagates through the mine, the flame may accelerate and transition into a detonation reaction if the criteria mentioned above are met.

## 2.2. SHOCK WAVE BEHAVIOR

The purpose of this thesis is to show how shock wave characteristics change as the wave propagates down the model under different tunnel scenarios. To do this, it helps to first discuss shock waves more generally. A shock wave is “a sharp change of pressure in a narrow region traveling through a medium, especially air, caused by explosion or by a body moving faster than sound” [19]. In the case of a detonation generated shock wave, the energy and gasses produced from the rapid exothermic reaction propagate a shock into the surrounding air. This shock is a sharp, nearly discontinuous, rise in pressure that travels away from the explosive source in all directions. Immediately behind the shock front is a region of high pressure called the positive phase. The positive phase is then followed by a period of lower than ambient pressure, the negative phase, which slowly equilibrates to pre-detonation ambient levels. The environment around the explosives has a notable effect on how the shock wave will propagate. The three environments that come up most often in explosives research are free air detonation, ground detonation, and shock tunnel detonation.

**2.2.1. Free Air Detonation.** A free air detonation, also called free-field or open-air detonation, is an explosive detonation that occurs where there are no surfaces around the charge to interact with the shock wave, i.e. in open air. In a free air detonation of a spherical explosive charge, the propagating shockwave will expand outward from the charge spherically, and the pressure versus time waveform can be modeled mathematically using the Friedlander equation. The waveform will start with a sharp rise to peak pressure, that exponentially decreases back to ambient pressure followed by an extended negative phase, that slowly rises back to ambient levels. An example waveform of the Friedlander curve is shown in Figure 2.2 while the numerical model for the curve is shown in Equation (1).

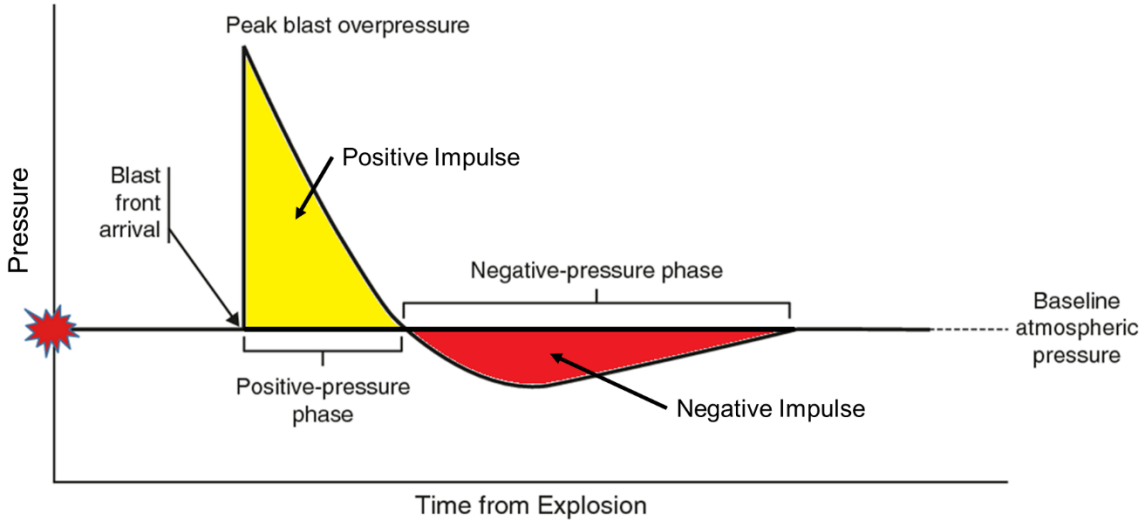


Figure 2.2: Typical Friedlander Waveform (Adapted from [21])

In Equation (1), P is the pressure at a fixed location, Ps is the peak pressure, t is the amount of time after the arrival of the shock front, and t+ is the total positive phase duration [20].

$$P = P_s e^{-\frac{t}{t^+}}\left(1 - \frac{t}{t^+}\right) \tag{1}$$

In addition to pressure, impulse is another characteristic that has a large effect on a blast waves' potential for causing damage or injury [22]. Impulse is defined as the integral of the pressure versus time function. This means that the impulse is equal to the area between the pressure curve and the x-axis, with units of pressure*time. Area above the x-axis is considered positive impulse and area below the x-axis is considered negative impulse, as illustrated in Figure 2.2.

An effective method for finding impulse from high fidelity pressure data is to use the trapezoid rule for definite integral approximation, shown in Equation (2). In this

equation, $t_0$ is the start time of the definite integral and $t_+$ is the end time of the definite integral. $P_i$ and $P_{i+1}$ are the pressures at the current and next time steps of the sum, and $t_i$ and $t_{i+1}$ are the time values of the current and next time steps for the sum.

$$I = \int_{t_0}^{t_+} P(t) = \sum_{i=t_0}^{t_+} \left(\frac{P_i + P_{i+1}}{2}\right) * (t_{i+1} - t_i) \quad (2)$$

**2.2.2. Surface Detonation.** When an explosive charge is initiated at or near ground level it is referred to as a surface detonation. In a surface detonation there is a single plane interfering with the travel of the shock wave, and that is the ground. When the shock wave interacts with the ground the energy will be effected in two main ways, some will be coupled with the ground, creating a crater and ejecting material, and some energy will be reflected off of the ground, back into the atmosphere. This reflected energy increases the effective air blast of most surface detonations to approximately 160% - 180% of the value from an equivalent free air detonation [23].

In a detonation where the explosive charge is in contact with the surface, there will be no distinction between the incident and reflected shock waves; the waves would immediately merge into a single semispherical shock front that would decay in the same manner as a free air detonation [24]. When there is distance between the charge and the surface, there will be separation between the incident and reflected shock waves after the incident wave impacts the surface. As the incident and reflected waves expand, the reflected wave will travel with a higher velocity through the already shocked medium and catch the leading incident wave, forming a single shock front known as the Mach stem.

The location where the incident wave, reflected wave, and Mach stem meet is called the triple point. Anything located above the triple point will experience two distinct pressure rises from the incident and reflected blast waves, while anything below the triple point will only experience a single, greater magnitude, pressure rise from the Mach stem [24]. Figure 2.3 provides two diagrams showing how a blast wave will expand from a surface detonation in contact with the ground and one that is elevated above the surface.

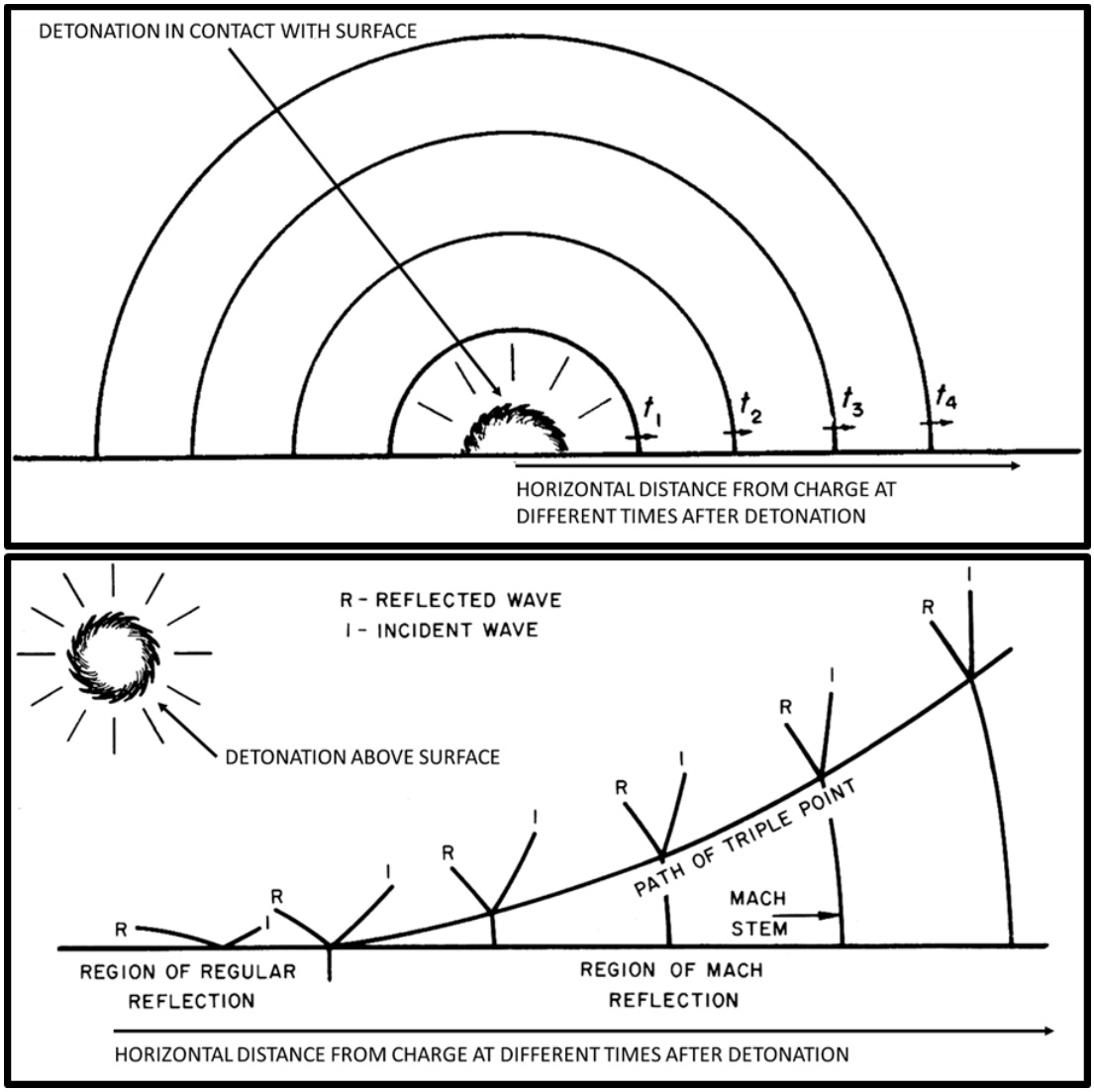


Figure 2.3: Shock Wave Propagation for Surface Detonations in Contact and Slightly Elevated from the Ground (Adapted from [24])

Surface detonations are often utilized in arena testing where a single charge is surrounded by multiple research targets at different distances away from the charge. This arena testing allows for multiple data collection points while only using a single detonation, since the blast wave will propagate symmetrically from the hemispherical charge. This maximizes the data collected while keeping explosive cost and number of tests as low as possible. Figure 2.4 shows an example arena test set-up.

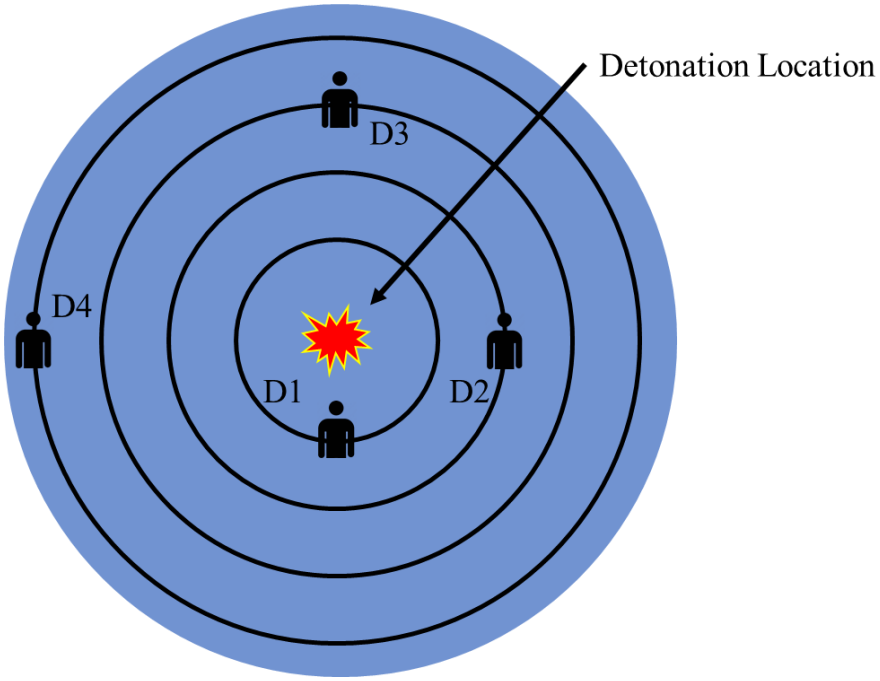


Figure 2.4: Arena Test Diagram

**2.2.3. Shock Tunnel Detonation.** Shock tunnels, or shock tubes, are tools used in research to study high velocity gas flow and the effect that flow has on objects. There are two main types of shock tunnels, compressed gas driven and detonation driven. Gas driven shock tunnels use a high-pressure driver gas, usually with low molecular weight like

hydrogen or helium, to create a shock in low pressure driven gas, typically air. The shock is usually created by rupturing a diaphragm that isolated the driver and driven gas segments of the tunnel [25]. Detonation driven shock tunnels use the expanding gases from an explosive detonation to propagate a shock wave and gas flow down the tunnel. In a detonation driven shock tunnel, the geometry of the tunnel confines the gas expansion and channels the energy down the length of the tube, illustrated in Figure 2.5. This leads to higher pressure and impulse creation with a smaller quantity of explosive. This energy channeling allows for simulation of larger arena style experiments with lower cost and smaller real estate [26].

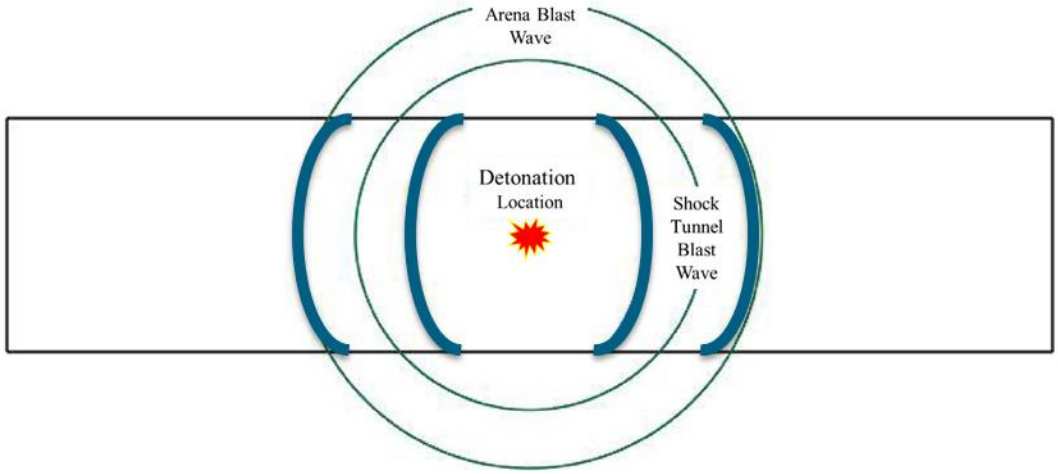


Figure 2.5: Shock Tunnel Blast Wave Diagram (Adapted from [27])

However, the use of detonation driven shock tunnels to simulate larger open area tests is not a perfect solution. Confining the expanding gases in the shock tube causes the pressure waveform to decay differently in shock tunnel testing than in arena tests. Specifically, there is longer than normal positive phase duration. This means longer blast

exposure for the object being tested and a larger impulse acting on the object [26]. This discrepancy between arena and shock tunnel testing can be helpful, allowing testing of blast loadings that are difficult to produce in open air, but also makes it more difficult to test objects under the exact forces they would experience in an arena test, like the one depicted in Figure 2.4, with multiple targets located at different distances from the blast epicenter.

The reason shock tunnels are so efficient at containing the energy from an explosion is because of the high impedance difference between the air inside the tunnel and the steel body around it. The large impedance difference causes nearly all of the energy from the shock wave to be reflected back into the tunnel with less energy being transmitted into the metal [28]. The shock reflected from the high impedance steel also increases the pressure [29] by the combination of the incident and reflected waves and this combination is termed the reflected pressure which may be up to 2x the incident pressure. More information on impedance and shock reflection can be found in Appendix C.

**2.2.4. Complex Confined Environments.** In addition to the traditional scenarios discussed above, previous research has been conducted on complex confined environments more like those tested in this thesis. These include various street designs that would be seen in an urban environment, and corner and intersection studies in tunnels that would relate to building corridors or mine drifts.

One study observed shock wave propagation in five common street scenarios: Crossroads, T-intersection, 90° bend, Straight Street, and Dead End. Pressure was recorded at four distances away from the charge in each of these scenarios, and impulse was calculated using the pressure vs time waveform data. This street configuration impulse data

was compared to the impulse data from an equivalent unconfined hemispherical airburst, which revealed that the confinement in the street scenarios led to a higher impulse than would be experienced from an unconfined air burst. Furthermore, as distance from the charge increased, so did the disparity in impulse between the confined and unconfined scenarios [30]. Figure 2.6 shows the five street configurations and the impulse ratio versus scaled distance graph that compares each street set-up to the equivalent open-air blast.

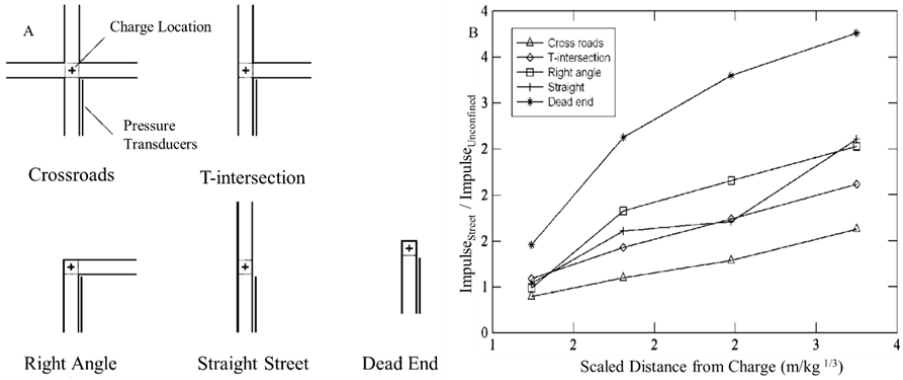


Figure 2.6: A. Street Configurations B. Street/Unconfined Impulse Ratio vs Scaled Distance (Adapted from [30])

In addition to the five street configurations, a 1:50 scale model was built of a more complex street layout to see how the shock wave propagates outside of the simple scenarios discussed previously. This model included buildings of different shapes and heights, meant to replicate the architectural diversity of a real city block. This testing resulted in a pressure trace that was very consistent between trials [30]. The waveform had multiple obvious peaks caused by the reflections from the cityscape. Figure 2.7 shows the layout of the small-scale cityscape and the pressure versus time waveform recorded at a pressure sensor. The graph shows the overlay of three trials.

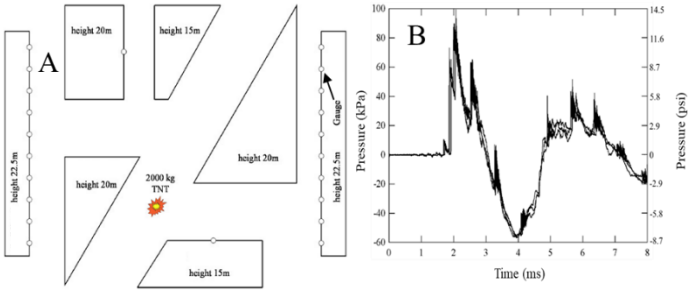


Figure 2.7: A. Cityscape B. Pressure vs Time Waveform (Adapted from [30])

Another study, by Igra et al., looked at the interaction between a planar shock wave and a 90° branched duct. This study showed that the diffraction of the shock wave around the corner results in nonstationary two-dimensional flow. The reflections created by the shock wave diffraction into the branched duct cause the wave to attenuate more quickly than it would in a straight duct [31]. Shadowgraph images of this phenomena were taken at four time steps during the diffraction event, showing the initial diffraction around the near corner, the reflection created off of the far corner, and the subsequent propagation of the initial and reflected shocks down both branches of the duct. Figure 2.8 shows these images labeled with their respective time stamps.

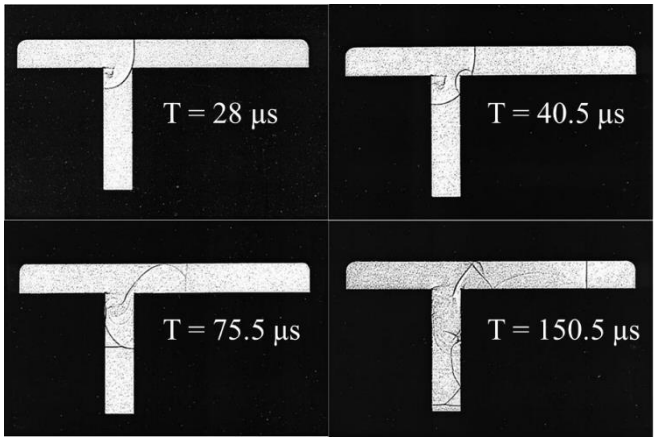


Figure 2.8: Shadowgraph Images of Planar Shock Wave Diffraction in a 90° Branched Duct (Adapted from [31])

A thesis by Morris investigated shock wave diffraction at an intersection for both open roof (urban environment) and closed roof (mine or hallway) environments. This testing was conducted using intersections with two different path widths, and multiple charge locations. Morris found that the enclosed environment led to higher pressures and impulses than were observed in the open top tests, but in the open tests the peak pressure and impulse was recorded closer to the charge, while in the enclosed scenario the shock wave did not produce its peak pressure and impulse until further away from the charge. The study also concluded that in both the open and enclosed tests, the narrow path width resulted in higher peak pressure and impulse than in corresponding tests using the wide path. Another difference observed between the open top and closed top tests was the degree of diffraction into the perpendicular street at the intersection. Morris reports that in the open roof tunnel, greater diffraction is seen when the charge is located closer to the intersection, but in enclosed tunnels greater diffraction is seen when the charge is detonated further down one of the paths [32]. A diagram of the experimental set-up for the near and far charge detonation scenarios is shown in Figure 2.9.

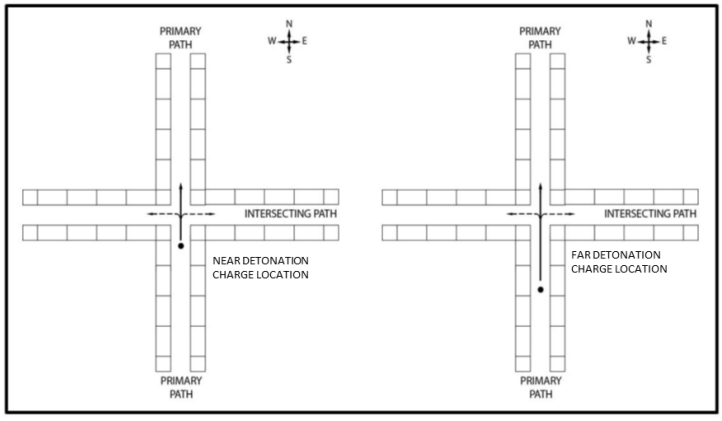


Figure 2.9: Near and Far Charge Location Diagrams (Adapted from [22])

## 2.3. MINE EXPLOSION INCIDENTS

Gas and dust explosions in coal mines have caused death and injury to miners and destruction of workings in all countries where coal is mined underground [33]. The first recorded mine explosion in the United States occurred at the Black Heath coal mine in Richmond, Virginia in March of 1839 [34]. Sources do not specify a cause for the explosion which killed 53 men, but based on the descriptions, it was very likely a methane initiated coal dust explosion [35]. While safety procedures implemented over the years have certainly slowed their frequency, dust explosions have continued to claim the lives of miners since this 1839 disaster.

Currently, coal dust explosions are most often caused when a pocket of methane gas is ignited by a spark from a continuous miner or other mining equipment. This methane explosion, often called a methane pop, lifts coal dust into the air. When this suspended coal dust is mixed with the right amount of oxygen, the flame from the methane pop will ignite the coal dust. The high surface area dust particles burn rapidly, and propagate the reaction down the mine, driving more coal dust in the air as it travels, further fueling the dust explosion [36]. The confinement of the tunnel in an underground coal dust explosion channels the explosive energy down the length of the tunnel. This confinement creates conditions to those found in shock tunnel tests, discussed previously, with longer positive phase durations and higher impulses than would be created from an equivalent open-air explosion.

Various steps have been taken to improve safety in coal mines and prevent these dust explosions. One of the most widely implemented safety practices is the spreading of inert rock dust throughout the mine. This rock dust serves two purposes. First, it provides

a layer on top of the coal dust that will ideally prevent the coal dust from going airborne after a methane pop. Second, if coal dust does make it into the air, the inert rock dust helps to absorb heat from the flame front, making it harder to ignite the coal dust and propagate through the mine [37]. In addition to laying out rock dust, miners have developed passive and active barriers to provide additional layers of protection. A common passive system, first developed by the Division of Mining Technology in South Africa, uses specially designed bags of rock dust that burst when exposed to the pressure of a coal dust explosion. This disperses more inert material into the air, supplementing the rock dust on the ground in extinguishing the burning coal dust [1]. Active barriers, such as the ExploSpot, use reservoirs of extinguishant, usually rock dust or dry chemical, that is propelled into the mine drift via compressed inert gas. These barriers are triggered by pressure or light sensors placed throughout the mine [38].

The first decade of the 20$^{th}$ century was the deadliest in U.S. underground coal mining, with 133 disasters leading to the deaths of 3,660 miners between January 1900 and December 1909 [39]. However, in more recent years, the United States coal industry has seen three of its safest decades, with one explosion causing 8 deaths between 1991 and 2000 and five accidents leading to 65 deaths between 2001 and 2010. There have been no major coal mine disasters recorded in the U.S. between 2011 and present (2020) [34].

While safety measures have undoubtedly reduced the frequency of coal dust explosions in the world's coal mines, recent disasters like the Sago Mine (2006) and Upper Big Branch Mine-South (2010) explosions show that more precautions still need to be taken. Combined, these accidents claimed the lives of 42 miners, and provide an incentive to find new ways of protecting personnel and equipment from future coal dust explosions

[34]. The maps in Figure 2.10 and Figure 2.11 show the approximate origin point and extent of flame propagation in the Sago and Upper Big Branch mine explosions respectively. For the Sago mine map, extent of coking is used as the metric for determining the area exposed to flames. Coal will react into coke when exposed to temperatures higher than 700°F in an oxygen deficient environment [40]. Flames were strongest in the areas with extra-large and large amounts of coking and were less intense in areas with small and trace amounts of coking.

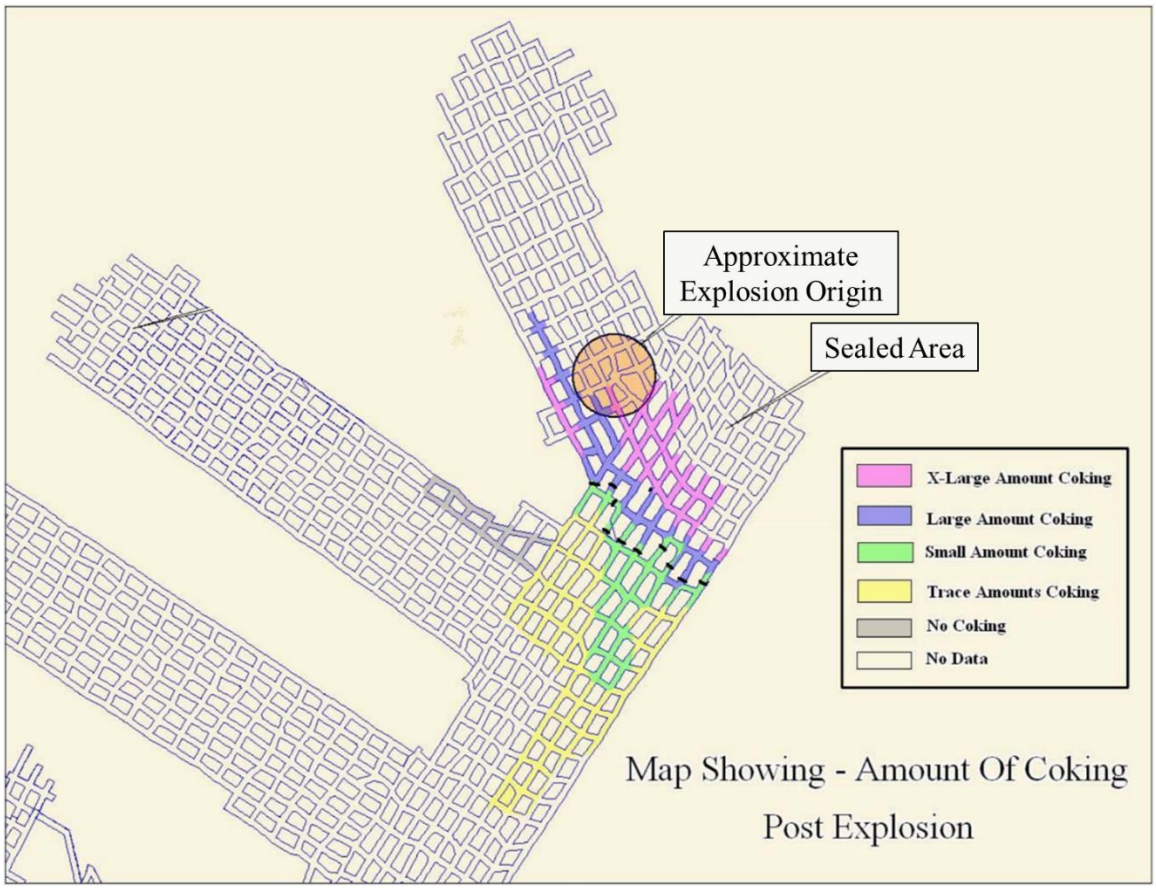


Figure 2.10: Sago Mine Explosion: Extent of Flame Map (Adapted from [40])

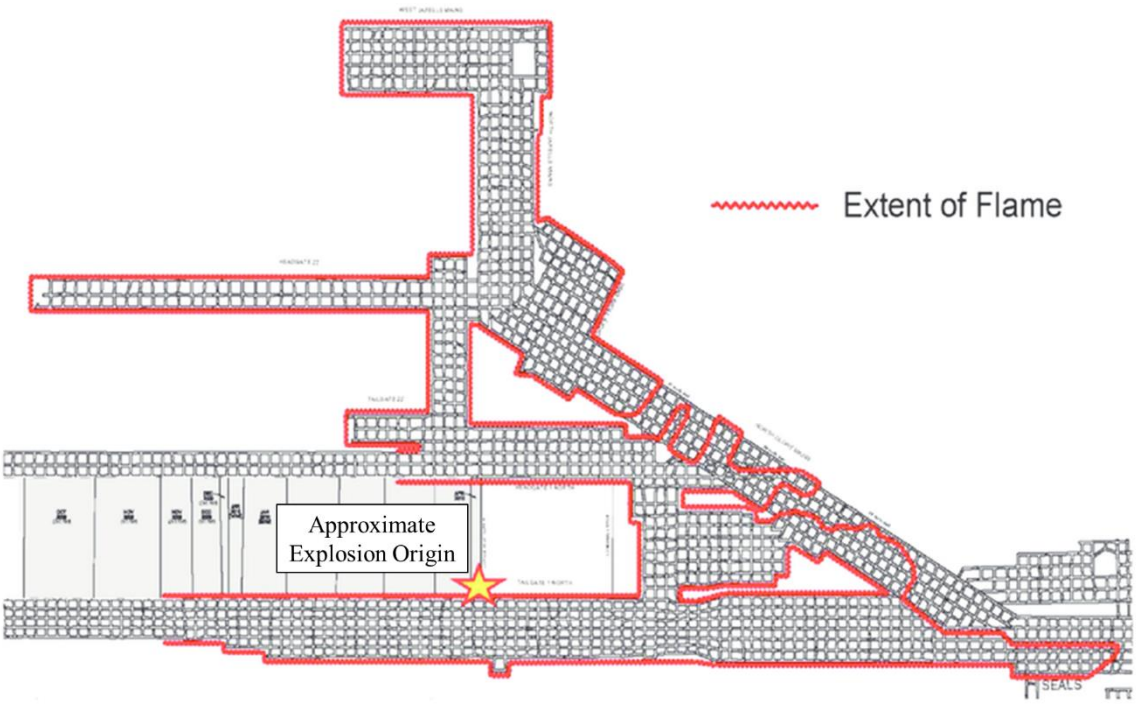


Figure 2.11: Upper Big Branch Mine Explosion: Extent of Flame Map (Adapted from [41])

## 2.4. URBAN EXPLOSIVE DISASTERS

The use of improvised explosive devices by terrorist groups or individuals creates a challenge for those tasked with countering terrorist activity. The size of these devices can range from something inside of a backpack to the entire cargo section of a van or truck, and often these explosives are used in city centers to damage or destroy buildings and cause great civilian casualties [42, 3]. There are many examples of these in recent history. The 1993 bombing of the World Trade Center in New York City, which killed six and injured over one thousand people, was perpetrated by a group that parked a van in the underground parking structure of the tower [2]. The van contained approximately 1,500lbs of urea nitrate and several cylinders of hydrogen gas [43].

The 1995 Oklahoma City bombing also involved a vehicle bomb. In this case a van was filled with 5,000lbs of ammonium nitrate and mixed with 1,200lbs of nitromethane to create an ammonium nitrate fuel oil explosive (ANFO) [44]. This attack killed 167 people and injured 684 [45]. In addition to the casualties, Figure 2.12 shows a map of the building damage caused by the blast from the truck bomb, with 35 buildings either collapsed or suffering structural damage and 312 with broken glass [46].

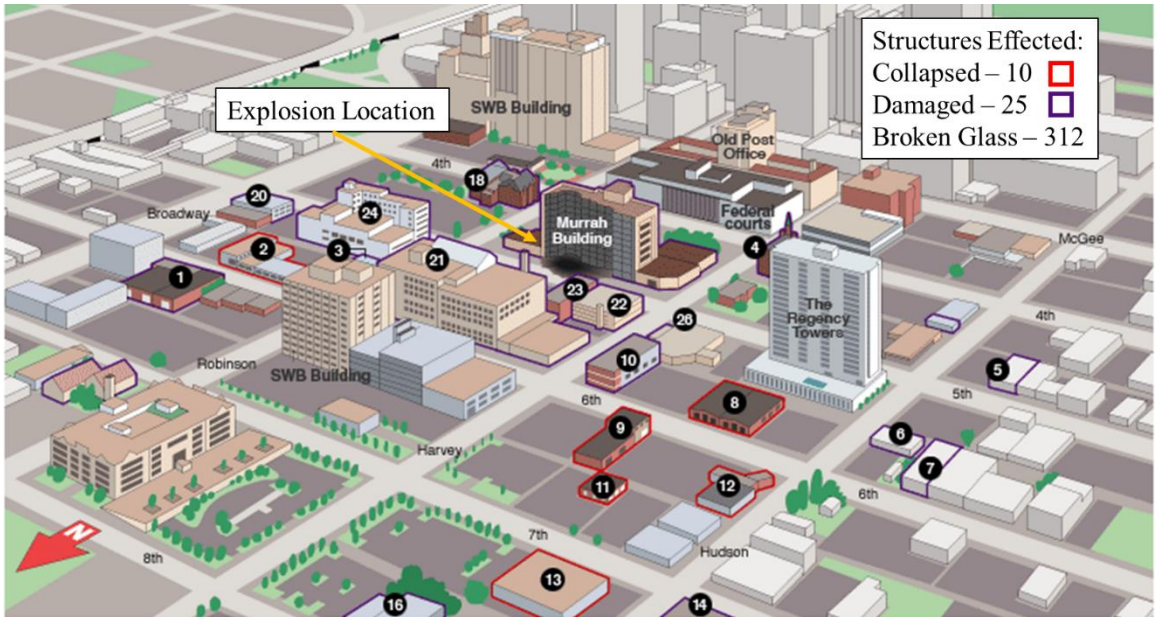


Figure 2.12: Oklahoma City Bombing Structural Damage Map (Adapted from [46])

More recently, the 2019 Sri Lanka Easter Sunday bombings of three churches and three hotels killed 321 people and injured more than 500 [4, 47]. The perpetrators of this attack used backpacks full of triacetone triperoxide (TATP) as the explosive devices to create this disaster [48].

In each of these cases the urea nitrate, ANFO, and TATP used were all high explosives, and the closely packed buildings in the city environments confined the energy from the explosion, causing shock wave reflections and channeling of the explosive energy down city streets which are the most open pathways available. The size, shape, and layout of the buildings will determine how the shock wave propagates through the environment, and where the high- and low-pressure areas will form as a result of shock channeling and diffraction.

Because of these and other incidents, tools like the Institute of Makers of Explosives Safety Analysis for Risk (IMESAFR) have been created. The primary purpose of this software is to calculate risk to personnel from explosives facilities, but tools like this can be expanded or developed to help determine risk and damage that would be caused from an explosion inside buildings and in urban areas [49, 50]. Research into blast resistant design is also being done to mitigate damage from urban bombings. This includes changes to landscape architecture to implement hard barriers that can physically prevent a large vehicle born explosive from getting too close to a building, as well as changes to structural design to improve the buildings response to shock loading. These changes include reinforcement of column to beam connections and the use of safer window material that is less prone to shattering than regular glass [51].

## 2.5. EXPLOSIVE BREACHING INJURIES

Since explosives were first utilized for combat, years of work has been done to try and better understand and improve treatment for injuries caused by explosives. Of course, the more obvious injuries, like loss of limb or laceration caused by flying debris or shrapnel

were most similar to traditional trauma injuries, and therefore could be treated using already understood methods. Injuries more specific to the shock wave produced from the explosive detonation, like ear drum and lung damage, took some specific research to better understand. This research produced data that correlated blast pressure and impulse to fatality from lung damage and likelihood of eardrum rupture, which has been used to improve protection for soldiers [52, 53, 54].

After these issues were better understood, focus shifted to injuries that were not immediately life threatening and took more time to observe, these being blast induced traumatic brain injuries (bTBI). Many studies focus on the chances of having different levels of brain damage based on peak overpressure and blast impulse from a single blast and how that injury develops and affects behavior over time [55, 56, 57]. Others look at the effects from repeated low-level blast pressures like those experienced by tank and artillery operators, soldiers using rocket propelled weapons, and explosive breaching personnel [58, 59]. Symptoms of this frequent exposure to subconcussive blasts include fatigue, memory loss, headaches, and slowed thought processes [60].

In the case of explosive breaching, the operators experience frequent shock wave exposure, and they are often detonating explosive charges in confined spaces, like the interior of a building. Like the mine tunnels and city streets discussed previously, the hallways and rooms inside a building confine the shock wave expansion from the explosive detonation, creating reflections and leading to higher pressures, positive phase duration, and impulse inside the building.

Procedures and tools are already in place to try and minimize the pressure experienced by breachers, such as special formations and blast shields (Figure 2.13). The

results of this thesis and future work like it can be used to improve these procedures by providing information on the places soldiers and officers should stand to feel the lowest blast pressure or alternatively places they should avoid to stay away from locally amplified pressures.

Figure 2.13: Soldier Formation and Blast Shield use for Explosive Breaching Training [61]

## 2.6. SCALING LAWS

When designing an experiment, it is often easier to conduct testing at a smaller scale than would be used in a real-world scenario. Small-scale tests can help mitigate a number of things, including testing costs, real estate required for the experiment, and the time it takes to set up repeat trials. In explosives testing, one of the greatest benefits of small-scale testing is the decreased safety risk in using smaller explosives charges. There

is always some risk when handling explosives, and proper handling techniques should be implemented to minimize the likelihood of an accident but keeping quantity small is an effective way to reduce the harm done if an accident does occur.

In order to design a small-scale experiment, proper scaling laws must be followed. This ensures that the results will still be meaningful when relating them to a full-scale scenario. The mine model built for this thesis is a 1:10 linear distance scaled model (i.e. 1 model ft = 10 full size ft). In explosives, a cubed root dimensional analysis scaling law coined "Scaled Distance" is used to compare charges of different sizes and at different distances from the pressure sensors. This scaled distance method is most often used in open air or surface detonation situations, but it has also been used to conduct small scale experiments in confined environments, like the five scale model scenarios used in this research. The previous small-scale experiments conducted in literature have stated that the cubed root scaling law is valid for their confined conditions, and therefore should provide reasonable accuracy for the purposes of this work [30]. The scaled distance equation is shown as Equation (3), where SD is scaled distance, R is the measured distance to the charge, and W is the charge weight [62].

$$SD = \frac{R}{W^{1/3}} \tag{3}$$

For the model mine to be representative of the full-scale setting, the scaled distance in the model and in the full size mine must be equivalent. This is laid out in Equation (4)

where $R_1$ and $W_1$ are the measured distance and weight for the full scale, and $R_2$ and $W_2$ are the measured distance and weight for the small-scale setup.

$$\frac{R_1}{{W_1}^{1/3}} = SD = \frac{R_2}{{W_2}^{1/3}} \tag{4}$$

This can be further rearranged to solve for $W_1$ as shown in Equation (5).

$$W_1 = ({W_2}^{1/3}(\frac{R_1}{R_2}))^3 \tag{5}$$

Based on the 1:10 distance ratio of the model $R_1/R_2$ equals 10, and assuming the 900mg base charge of the blasting cap used in these experiments provides the majority of the explosive energy $W_2$ = 0.9g. Plugging these values into Equation (5) a solution can be calculated showing that $W_1$ = 900g. So, to replicate these small-scale experiments in a full-scale scenario, a 900g, or 0.9kg, charge of RDX would need to be used. This charge size provides a good parallel to breaching charges like the Gatecrasher which can have a net explosive weight between 300g and 3kg, and the M112 Composition C4 block charge which is about 570g [63, 64].

## 2.7. BACKGROUND SUMMARY

Explosive materials are capable of releasing large amounts of energy and expanding gases in a short period of time. Explosives have varying reaction rates and sensitivity to stimulus, which make different explosives more useful in certain situations than others.

High explosives react more violently and have a higher brisance than low explosives, giving them a greater potential for causing damage than the same amount of low explosive. Secondary explosives are less sensitive to stimulus and therefore can be handled more safely than primary explosives.

The environment where an explosive is detonated has a significant effect on how the shock wave resulting from the detonation will propagate. In an open-air scenario, the shock wave will expand in all directions and dissipate. As more confinement is introduced in the form of walls or the ground, the interaction between the shock wave and these barriers create shock reflections as well as shock channeling and diffraction effects which determine how the wave propagates in the enclosed space.

Mine tunnels, urban areas with high building density, and the interior of buildings, are some examples of enclosed spaces where explosives are initiated. Small scale testing is an effective way to study shock propagation in these environments in a controlled manner. The small-scale environment allows for tests that consume fewer resources but provide data that is applicable to full scale scenarios.

# 3. METHODOLOGY

Testing for this thesis consisted of building a small-scale model, instrumenting the model such that high-fidelity pressure data could be recorded, and initiating an explosive inside the model so that shockwave propagation could be observed. The explosives used in this testing were Austin Powder RockStar electric detonators because they provided a consistent shock wave for multiple test trials, and they allowed for easy and safe initiation inside the model. The small-scale model built for this thesis is based on an experimental mine at the Missouri University of Science and Technology, and because of this, mining terminology such as portal, pillar, and drift, is often used to describe the geometry of the model and its different tunnel variations. Even though this mining vocabulary is used, the results of the testing are still very applicable to explosive breaching and urban bombing scenarios.

## 3.1. DESIGN OF SCALE MODEL

The small-scale mine model designed and built for this thesis is based on the WOMBAT mine workings at the Missouri University of Science and Technology circa summer 2018. The design was modified from the WOMBAT map to have three drifts and extra crosscuts so that a greater variety of tunnel designs could be tested. The drawing of this model, as well as its dimensions in inches, is shown in Figure 3.1. The model is 5ft wide, 20ft long, and 1ft tall. All three drifts have a cross-section of 12in x 11.67in. The pillars are all 12in tall and 12in wide, but with varying lengths. Unless shown otherwise, the crosscut width between pillars is 14in.

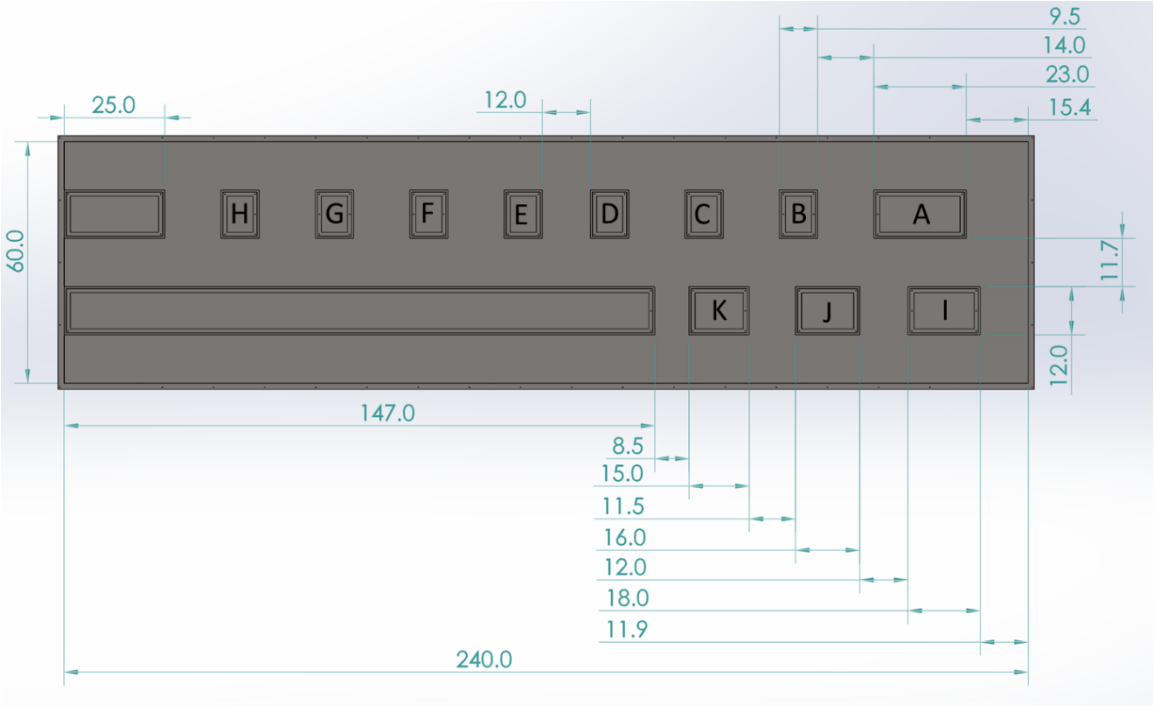


Figure 3.1: Mine Model Dimensions (Inches)

The floor, walls, and pillars in the model were constructed from ½ in thick carbon steel. The roof of the model was comprised of three ½ in. thick polycarbonate sheets in order to cover the entire model, including one 4 ft. x 5 ft. sheet and two 8 ft. x 5 ft. sheets. These polycarbonate sheets were bolted down to flanges on the top of the pillars and walls of the model, with large washers to distribute the explosive load as evenly as possible. Stoppings to block crosscuts were cut from ¼ in. thick carbon steel bar stock and were bolted to the necessary pillars to create various tunnel designs. The model was attached to legs, supporting it at a 60° angle with the ground. This angled layout was chosen to provide a good viewing angle for the high-speed cameras used to record the testing. Figure 3.2 shows a photo of the model set for the Straight-line tunnel tests, with stoppings and polycarbonate roof in place. Figure 3.3 shows the rear of the model and highlights the legs that were constructed to hold up the structure.

Figure 3.2: Scale Model Photo (In-front)

Figure 3.3: Scale Model Photo (Behind)

To protect the polycarbonate roof from the heat of the detonation and the blasting cap case fragments, a blast box was constructed out of ¼ in. carbon steel. This blast box could be removed from the model without removing the polycarbonate roof, which made for quicker resets between trials. Two flanges were welded inside the blast box to ensure

the blasting cap was placed in the same location for each test. The blasting cap was held by a square piece of foam insulation, cut from a template so the pieces would repeatedly fit snugly within the blast box. This foam piece rested against the flanges, fully defining the location of the explosive for each test. When the charge was set, the blast box was inserted and bolted into the model, securing it for each test. Images of the blast box and foam charge holder are shown in Figure 3.4.

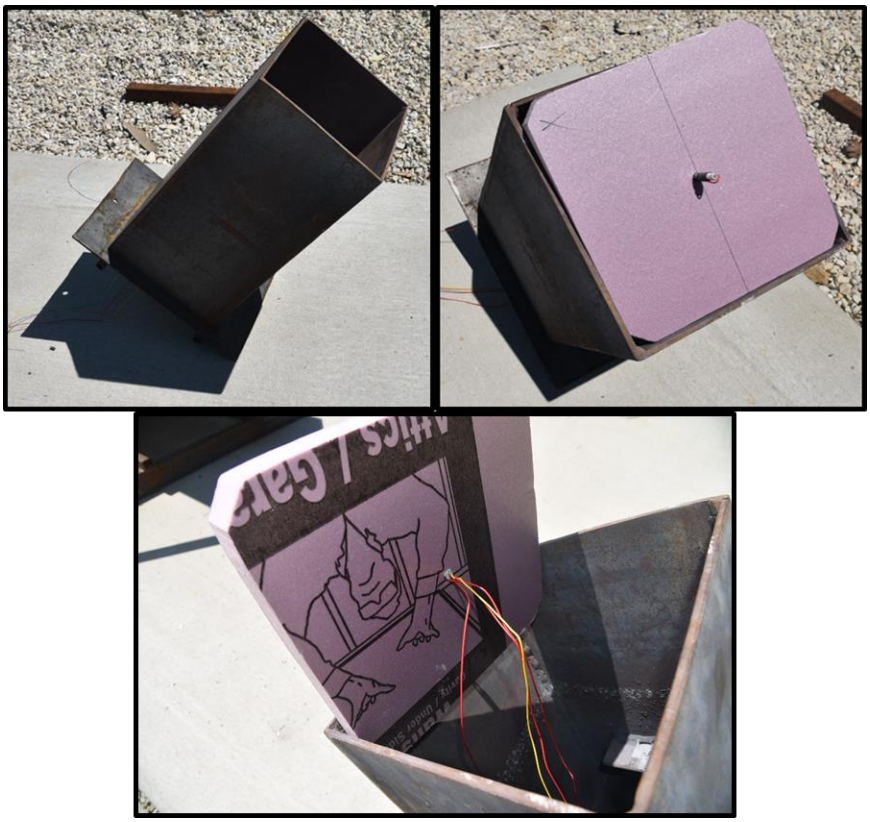

Figure 3.4: Blast Box and Foam Charge Holder

## 3.2. INSTRUMENTATION

The instrumentation used in these experiments included an array of pressure sensors and a high-speed camera. The pressure sensors were essential to tracking the properties of the blast wave as it traveled down the model, and the high-speed video helped to provide a visual correlation to the data from the pressure sensors.

The sensors used in the testing were a combination of PCB Piezotronics 102B04 and 102B15 high-frequency ICP® pressure sensors (flush mount sensors). The 102B04 and 102B15 sensors have a measurement range of up to 1000psi and 200psi respectively, with a rise time of less than 1 µs. These pressure transducers were connected to a Hi-Techniques Synergy P Data Acquisition System (DAS) with a sampling rate of 2,000,000 Hz (samples/second). The camera used to record high-speed video of these tests was the Phantom v2012, a monochrome high-speed imaging camera capable of capturing 22,500 frames per second (fps) at full resolution of 1280x800, and over 600,000 fps at lower resolutions.


Figure 3.5: PCB Flush Mount Sensor(A), Phantom v2012 Camera(B), and Hi-Techniques Data Acquisition System(C) [65] [66] [67]

### 3.3. TEST MATRIX

There were five designs that were tested in the small-scale mine. All of these designs utilized an Austin Powder RockStar Detonator blasting cap to provide the shock wave that was observed and recorded by the high-speed camera and pressure sensors. This electric blasting cap was chosen as the explosive source for this testing because it provided consistent shockwave formation between tests. Additionally, it acts as a good small-scale analog for the high explosives used in explosive breaching and urban bombings. While the point source high explosive detonation of the blasting cap is not as close of a match for the pressure waveform profile seen in coal dust explosions, the increased consistency of this manufactured product provided better data for analysis than was collected from initial testing with small-scale dust explosions.

The RockStar detonators used in this testing contain a combination of both primary and secondary high explosives, using a small quantity of primary explosive to initiate a larger base charge of secondary explosive. The firing current, produced by a Scorpion blasting machine, ignites the 300mg lead(II) azide primary explosive which quickly undergoes a deflagration to detonation transition. The shock from the detonating primary explosive then initiates the 900mg main charge of RDX and/or PETN secondary explosive [68, 69]. This explosive device is typically used as the first step in a larger explosives train, meant to start the detonation of a larger mass of secondary explosive. However, with the scaled-down environment of this test, the blasting cap provided sufficient energy to propagate a shock wave in air down the length of the model without over pressuring the system and breaking fasteners or the polycarbonate roof.

For each test design, flush-mount sensors were placed in areas of interest, with some sensors in the floor at intersections, and others placed in the center of the face of certain pillars. This sensor location would be analogous to the wall of a corridor for an indoor breaching scenario, or the outside face of a building in an urban bombing situation. In addition to the corner and intersection sensors, one sensor was placed in the floor of the model just before the exit to study how the overall waveform of the pressure pulse is affected by the different test scenarios.

Figure 3.6 - Figure 3.10 show the tunnel diagrams for the five test scenarios analyzed in this thesis. In each figure, the red and yellow cloud indicates the point of initiation, the black lines and dots represent pillar and floor sensors respectively, and the yellow lines indicate the stoppings used to create the pathways. Sensor labels were kept consistent through each design and can be found in Figure 3.10, since the Split Around Pillar design utilized all sixteen sensors. Floor sensors are labeled as Base1 through Base7 and pillar sensors are labeled with the pillar letter followed by a number (i.e. F2 is the second sensor on Pillar F). Each tunnel scenario was tested six times and a breakdown of which sensors are used in each design is shown in Table 3.1.

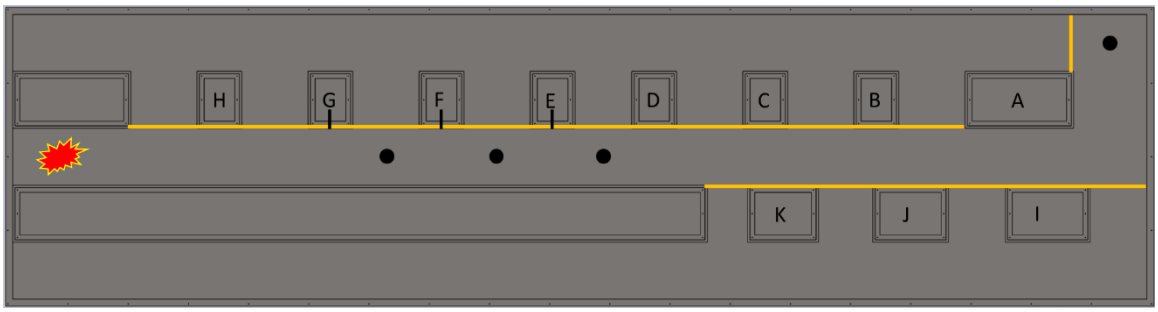


Figure 3.6: Design 1 - Straight-line

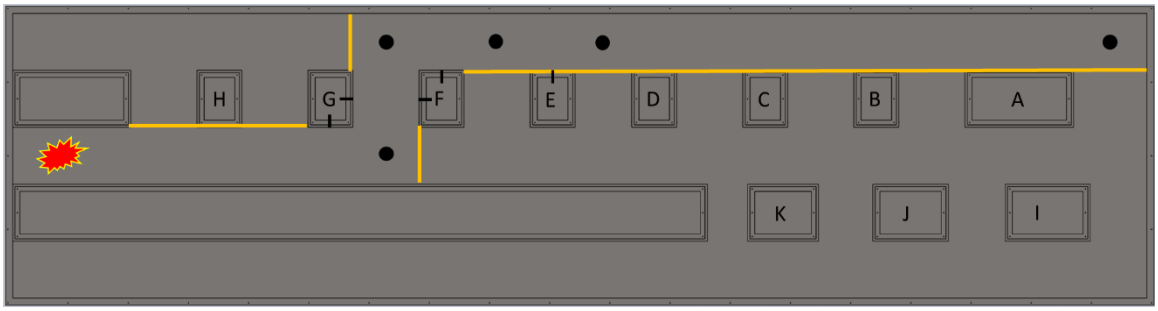


Figure 3.7: Design 2 - Single Turn

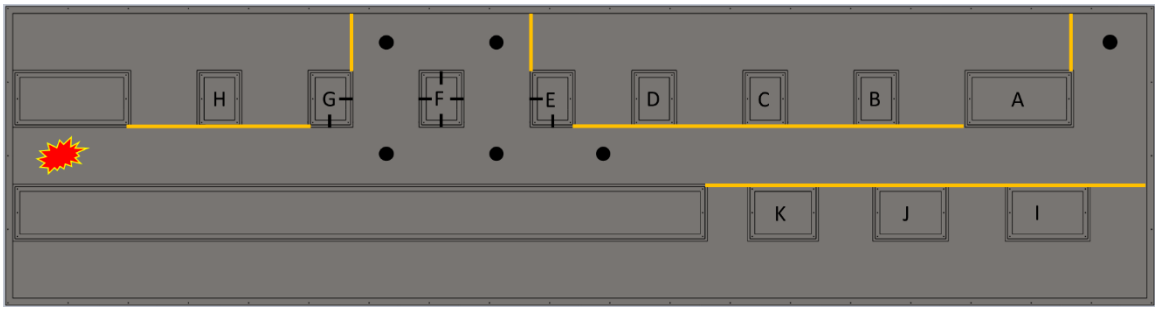


Figure 3.8: Design 3 - Around Pillar

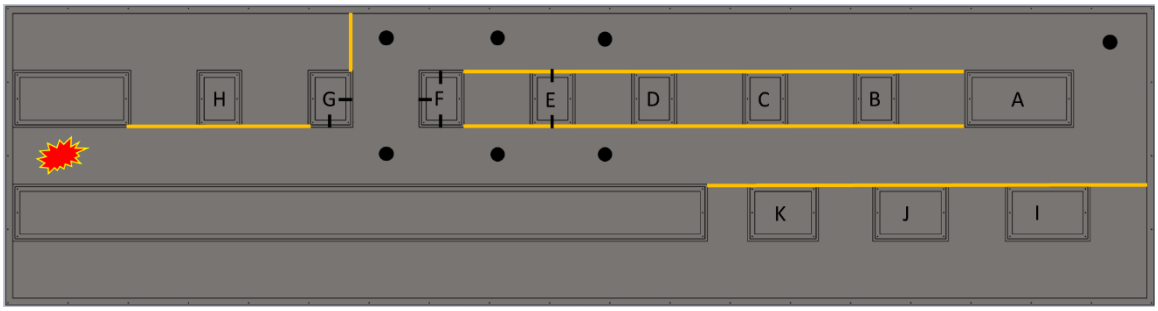


Figure 3.9: Design 4 – Split

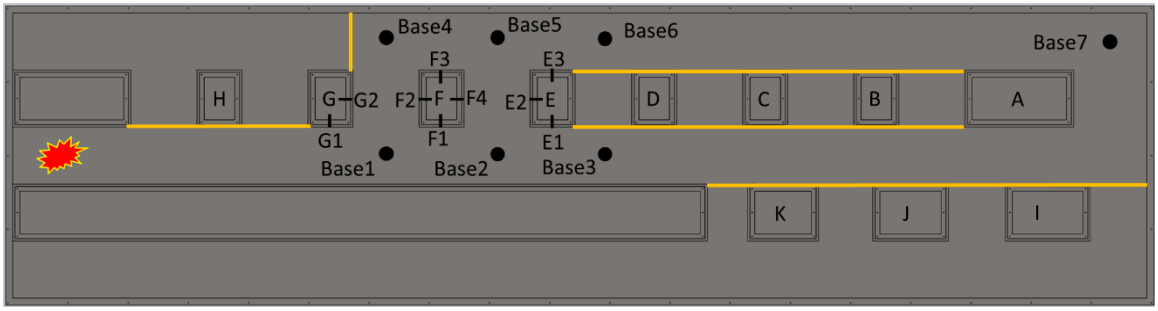


Figure 3.10: Design 5 - Split Around Pillar

Table 3.1: Sensor Position Breakdown (Sensor descriptions in Section 3.2)

| | Straight-line | Single Turn | Around Pillar | Split | Split Around Pillar |
|---|---|---|---|---|---|
| Trials | 6 | 6 | 6 | 6 | 6 |
| Base1 | 102B04 | 102B04 | 102B04 | 102B04 | 102B04 |
| Base2 | 102B04 | - | 102B04 | 102B04 | 102B04 |
| Base3 | 102B15 | - | 102B15 | 102B15 | 102B15 |
| Base4 | - | 102B15 | 102B15 | 102B15 | 102B15 |
| Base5 | - | 102B15 | 102B15 | 102B15 | 102B15 |
| Base6 | - | 102B15 | - | 102B15 | 102B15 |
| Base7 | 102B15 | 102B15 | 102B15 | 102B15 | 102B15 |
| G1 | 102B04 | 102B04 | 102B04 | 102B04 | 102B04 |
| G2 | - | 102B15 | 102B15 | 102B15 | 102B15 |
| F1 | 102B04 | - | 102B04 | 102B04 | 102B04 |
| F2 | - | 102B04 | 102B04 | 102B04 | 102B04 |
| F3 | - | 102B15 | 102B15 | 102B15 | 102B15 |
| F4 | - | - | 102B15 | - | 102B15 |
| E1 | 102B15 | - | 102B15 | 102B15 | 102B15 |
| E2 | - | - | 102B15 | - | 102B15 |
| E3 | - | 102B15 | - | 102B15 | 102B15 |

# 4. RESULTS AND ANALYSIS

The data from the six trials in each design were analyzed to find the peak pressure, maximum impulse, and rise time at each sensor for each test. For this thesis, maximum impulse is defined as the maximum value of the integral of the pressure curve over a 20 ms period, beginning at the start of the positive phase. Typically, impulse is calculated through the end of the positive phase, but with the many reflection peaks in the data from these tests, the end of the positive phase was difficult to manually determine at most sensors. The 20ms window was used because it encompassed the maximum impulse value for all pressure traces, and it was these maximum impulse values that were desired for the analysis. For the analysis in this thesis, impulse was calculated using the trapezoidal rule for definite integral approximation. The start of the positive phase is defined here as the time at which pressure equals zero immediately before the rise in pressure due to the detonation. Peak pressure and maximum impulse recorded from the sensors were averaged across the six repetitions for each of the five design layouts. These averages were used to compare data within and between designs. The peak pressure and maximum impulse recorded by the sensors for each of the six trials of the different tunnel designs are presented in tables in Appendix A. Appendix A also shows the mean, standard deviation, and 95% confidence interval for each sensor. Figure 4.1 shows these parameters on a pressure trace from Test 1 of the Straight-line scenario at the Base1 pressure sensor. The area between the x-axis and the pressure trace is the impulse for the pressure wave. The area above the x-axis, shaded in yellow, is positive impulse, and the area below the x-axis, shaded in red,

is negative impulse. Figure 4.2 shows how impulse changes with time for this example pressure curve, and the maximum impulse is labeled in that figure.

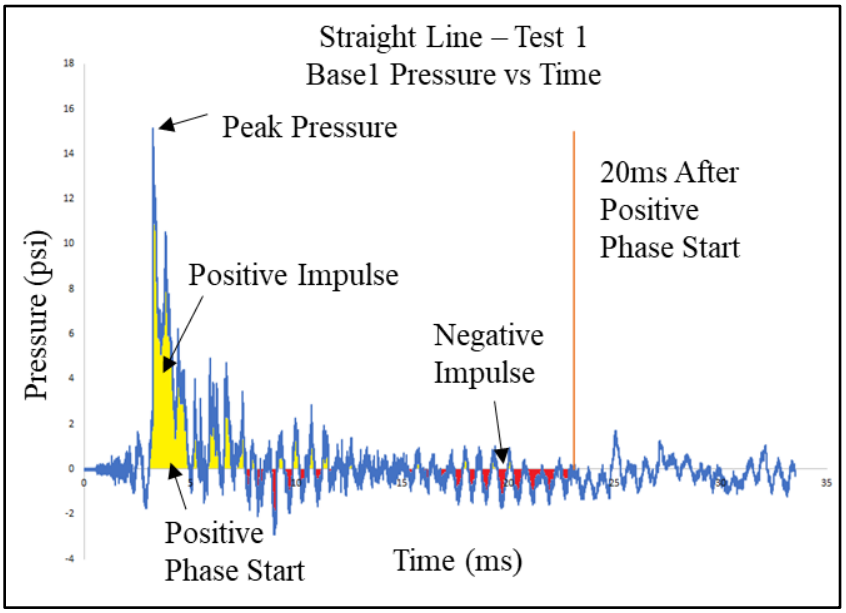


Figure 4.1: Labeled Pressure Trace

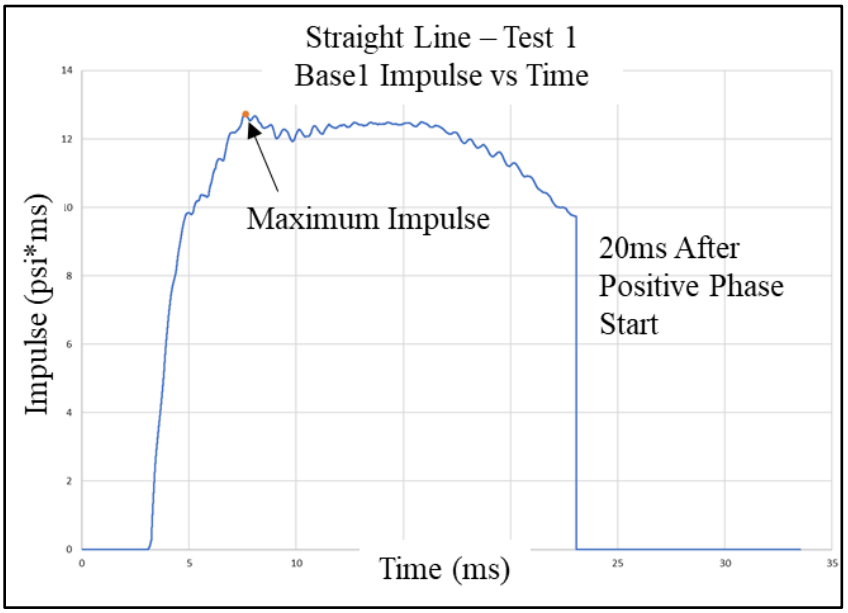


Figure 4.2: Labeled Impulse Trace

## 4.1. BLAST WAVE BEHAVIOR IN EACH TUNNEL DESIGN

**4.1.1. Straight-line.** The straight-line design acts as the control for this experiment. This set-up shows how the shock wave travels down a single drift with no obstructions or change in direction, as shown in Figure 3.6 in Section 3.3 - TEST MATRIX. This tunnel design utilized seven pressure sensors, and the data collected at these sensors is presented below in Table 4.1. This table presents the average peak pressure and average maximum impulse at every sensor for the Straight-line scenario.

Table 4.1: Straight-line Average Peak Pressure and Average Maximum Impulse

| Sensor | Peak Pressure (psi) | Maximum Impulse (psi*ms) |
|---|---|---|
| BASE1 | *15.12* | *13.06* |
| BASE2 | *9.98* | *12.96* |
| BASE3 | *8.42* | *11.19* |
| BASE7 | *5.16* | *7.01* |
| G1 | *13.76* | *13.29* |
| F1 | *11.53* | *12.80* |
| E1 | *9.53* | *11.73* |

To better visualize the data provided in this table, Figure 4.3 and Figure 4.4 were created. These figures show the data from Table 4.1 as a percentage of the value recorded at sensor G1. This makes it easier to see how the properties changed as the shock wave propagated, by comparing everything to the sensor closest to the blast. For example, Figure 4.3 shows a 100% peak pressure at sensor G1 which, after a small rise at Base1, trends down to 61% at sensor Base 3. Finally, the figure shows that the pressure just before the exit at Base 7 is 38% of the pressure from G1, a 62% decrease in pressure between the first sensor and the portal of the mine model.

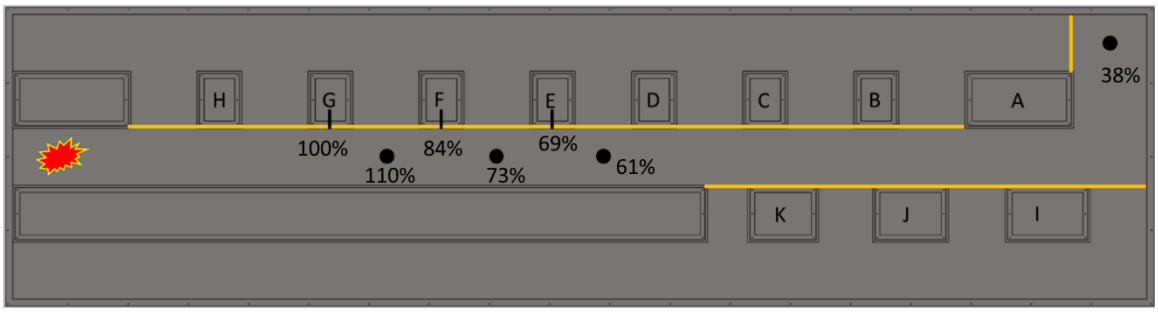


Figure 4.3: Straight-line Peak Pressures with respect to Sensor G1

Similarly, Figure 4.4 shows the maximum impulse as a percentage of the G1 value. This figure shows that the impulse decreases at a much slower rate than seen with the pressures in Figure 4.3, since the impulse only drops from 100% to 84% in between sensors G1 and Base3, staying above 90% all the way to E1. This can be explained by looking at the pressure waveforms for this scenario in Appendix B. These graphs show that reflections in the tunnel produce many low intensity high-frequency spikes in pressure for a few milliseconds after the main positive phase pressure spike has abated. These small pressure reverberations continue to increase the impulse, resulting in the high impulse percentages shown in Figure 4.4.

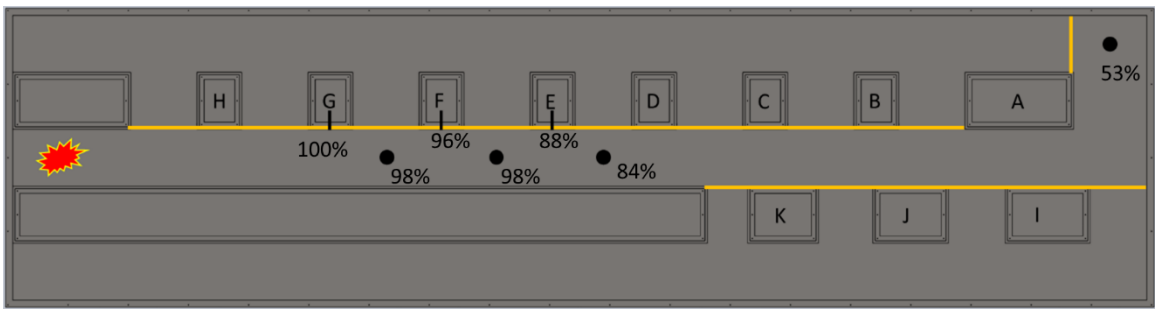


Figure 4.4: Straight-line Maximum Impulses with respect to Sensor G1

This higher, longer lasting impulse, is consistent with the findings in more traditional shock tunnel and urban environment studies, as discussed in Section 2.2. The previous research shows that the confinement of the enclosed space leads to longer positive phase durations which ultimately result in higher impulse values. There was still a significant drop in impulse between the first and last sensor with the impulse at Base7 being nearly half the impulse at G1.

**4.1.2. Single Turn.** The next scenario tested was the Single Turn design, shown in Figure 3.7. This tunnel design consists of two forced ninety-degree turns creating a path between the center drift and the top drift, connected by a crosscut. This configuration uses ten pressure sensors to record all the necessary data. As with the straight-line presented above, Table 4.2 contains the pressure and impulse data for the single turn tunnel, while Figure 4.5 and Figure 4.6 show the values as a percentage of sensor G1, allowing for better visualization of trends.

Table 4.2: Single Turn Average Peak Pressure and Average Maximum Impulse

| Sensor | Peak Pressure (psi) | Maximum Impulse (psi*ms) |
|---|---|---|
| BASE1 | *14.34* | *11.88* |
| BASE4 | *8.75* | *11.22* |
| BASE5 | *6.16* | *10.04* |
| BASE6 | *6.24* | *9.96* |
| BASE7 | *6.46* | *8.10* |
| G1 | *12.80* | *11.63* |
| G2 | *10.04* | *11.76* |
| F2 | *10.07* | *10.63* |
| F3 | *8.77* | *10.47* |
| E3 | *8.25* | *10.12* |

The key takeaways from the single turn test are the significant pressure drop observed around both corners and the unexpected similarity between the data at G2 and F2. Once again, a slight increase in pressure is recorded between G1 and Base1, followed by a 32% decrease in pressure between G1 and Base4 as the blast wave makes the first corner. Less drastically, an additional 20% pressure decrease is seen between G1 and Base5, bringing the pressure down to 48% of its original intensity as the wave develops in the upper drift.

An additional aspect to note here is the 78% and 79% values at G2 and F2 respectively. Going into this test, it was expected that G2 would have a significant drop in pressure because the sensor is on the back side of pillar G and the wave would have to travel around the corner before affecting the sensor. However, with this forced corner, a significant amount of the energy is reflected off the stopping and pillar F, such that the pressures at G2 and F2 are nearly identical.

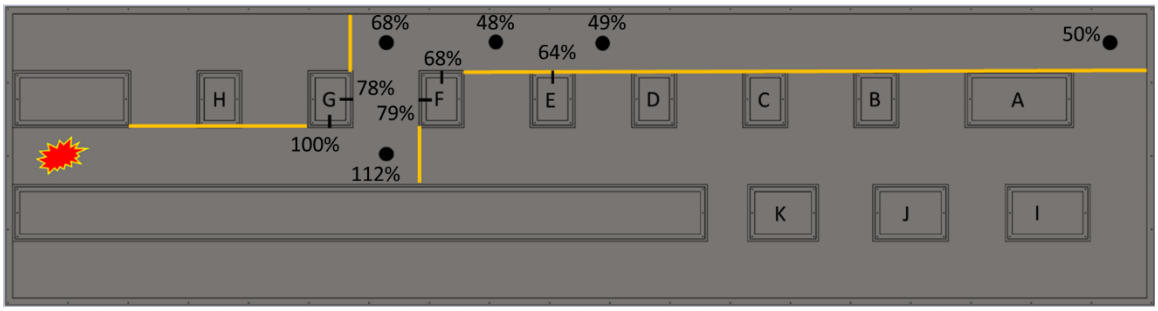


Figure 4.5: Single Turn Peak Pressure with respect to Sensor G1

Looking at Figure 4.6, the illustration shows that impulse again decreases at a slower rate than peak pressure. This is consistent with the results of traditional shock tunnel

testing and the street configuration studies discussed in Section 2.2. Similar to the discussion of the Straight-line test (Section 4.1.1), these high impulse values appear to be an effect of pressure wave reflections off of the walls of the model. In particular, the impulse maintains high values through both corners, staying above 90% of the G1 value until reaching sensor Base5 in the upper drift. This seems to be a product of especially large reflections recorded at the G2 and F2 sensors in the crosscut. In fact, the data shows the impulse at G2 to be greater than that recorded at F2, further disproving the presumption that being on the backside of the G pillar would provide protection from the effects of the blast wave.

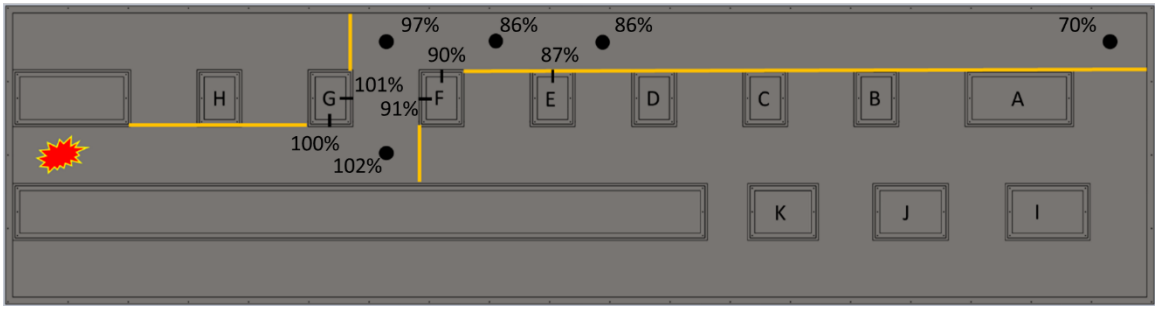


Figure 4.6: Single Turn Maximum Impulse with respect to Sensor G1

**4.1.3. Around Pillar.** The third tunnel design analyzed here is the Around Pillar pathway. This pathway consists of the middle drift with an open path around pillar F that connects back to the middle drift. This set-up utilizes fourteen pressure sensors. The diagram for this scenario is shown in Figure 3.8 in Section 3.3. Table 4.3 provides the peak pressure and maximum impulse data for the Around Pillar testing.

This design shows some of the differences between the forced corners in the single turn set-up and the intersections seen here. It also emphasizes how a dead route, one that does not direct flow back to the portal, can act as an energy sink and decrease the pressure of the wave further down the drift, and especially at the tunnel exit.

Table 4.3: Around Pillar Average Peak Pressure and Average Maximum Impulse

| Sensor | Peak Pressure (psi) | Maximum Impulse (psi*ms) |
|---|---|---|
| BASE1 | *12.42* | *11.52* |
| BASE2 | *7.82* | *11.44* |
| BASE3 | *5.31* | *10.33* |
| BASE4 | *5.48* | *10.51* |
| BASE5 | *7.94* | *12.50* |
| BASE7 | *2.84* | *5.00* |
| G1 | *14.70* | *11.96* |
| G2 | *5.77* | *9.76* |
| F1 | *9.04* | *13.29* |
| F2 | *9.23* | *12.36* |
| F3 | *5.81* | *11.54* |
| F4 | *5.06* | *11.68* |
| E1 | *7.77* | *11.25* |
| E2 | *6.77* | *11.94* |

Figure 4.7 shows the pressure data above on the Around Pillar diagram as a percentage of the G1 value. The first thing to notice is the pressure value at G2; it is only 39% of the initial G1 pressure and is 38% smaller than the pressure experienced at sensor F2 on the opposite side of the crosscut. This contrasts with the Single Turn testing where the pressure values for G2 and F2 were nearly identical and had only dissipated about 20% from the G1 value. This highlights the difference between a corner and an intersection. When the wave can keep traveling in the same direction, the crosscut sees less pressure,

and the difference between the close and far wall of the crosscut, sensors G2 and F2, become more pronounced. Interestingly, sensor Base5 experienced an amplification effect, with a pressure higher than either sensor immediately before it, at 54% of the pressure at G1. The pressure waves from the GF crosscut and the FE crosscut collide in the closed corner creating a high-pressure point in the channel around pillar F.

In addition to showing the different effects from intersections and corners, the data shows that the closed channel around pillar F removes much of the energy from the wave that continues down the central drift. The pressure at Base3 is only 36% of that at G1, which is much lower than the 61% pressure at Base3 observed in the Straight-line control tests. Similarly, the 19% exit portal pressure is half the strength of the Straight-line Base7 value, relative to each test's G1 pressure.

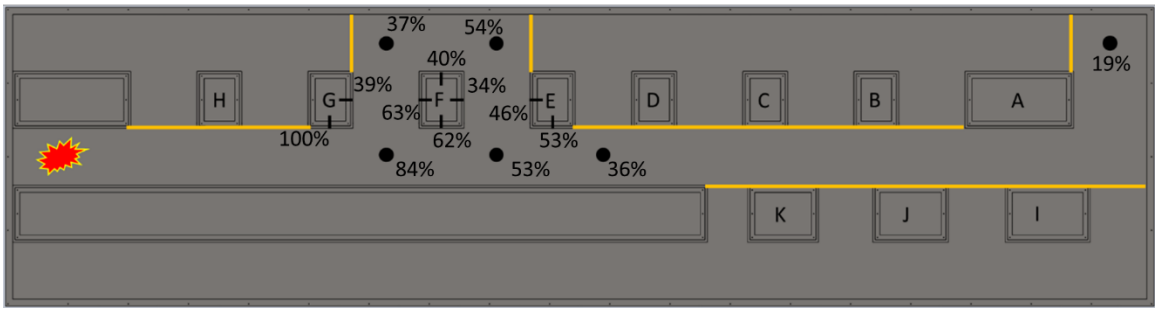


Figure 4.7: Around Pillar Peak Pressures with respect to Sensor G1

The impulse results are quite different than the pressure results for this Around Pillar test. Figure 4.8 shows the maximum impulses remain quite high until after the FE crosscut. Except for G2 and Base4, all impulse values remain above 95% until sensor E1. This may be related to the energy sink effect that was discussed in the pressure analysis

above, and the wave convergence at sensor Base5. The wave pressures are lower than in the center drift, but with opposite flow directions and many reflective surfaces around the channel, the positive phase duration becomes longer. This leads to high impulses, and a large portion of the blast energy getting trapped and dissipated within the channel around pillar F instead of propagating down the center drift and out the portal.

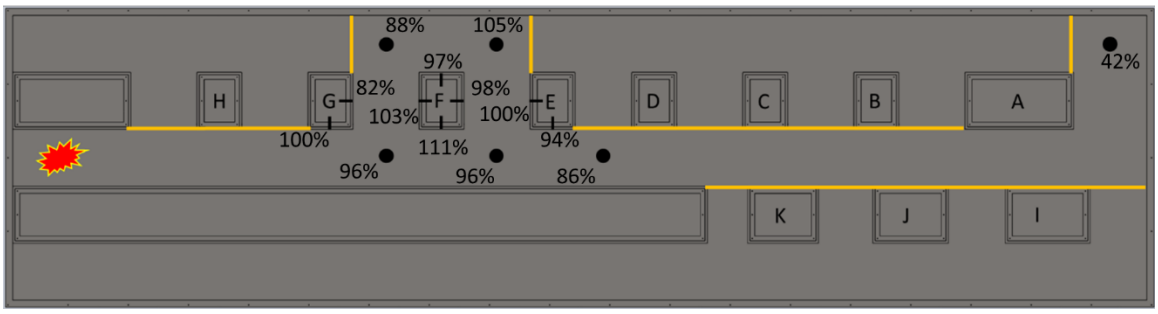


Figure 4.8: Around Pillar Maximum Impulse with respect to Sensor G1

**4.1.4. Split.** The Split tunnel design, shown in Figure 3.9, simulates a scenario where a crosscut connects the center drift to the upper drift, and both of these lead to the portal. This test utilizes fourteen sensors to measure pressure down both drifts, at the crosscut, and at the exit of the model. The average peak pressures and maximum impulses for the Split scenario are shown in Table 4.4.

The data from the split tunnel shows similarities to the Around Pillar test, specifically at the GF intersection. This helps to confirm the data from the Around Pillar test (Section 4.1.3) and shows that the amount of pressure experienced at the intersection is consistent in different tunnel designs. However, there is also a key contrast in the pressure and impulse experienced at the Base7 exit sensor.

Table 4.4: Split Average Peak Pressure and Average Maximum Impulse

| Sensor | Peak Pressure (psi) | Maximum Impulse (psi*ms) |
|---|---|---|
| BASE1 | *11.90* | *8.72* |
| BASE2 | *7.53* | *9.18* |
| BASE3 | *6.46* | *8.44* |
| BASE4 | *5.70* | *7.68* |
| BASE5 | *4.60* | *7.17* |
| BASE6 | *3.77* | *7.87* |
| BASE7 | *5.56* | *7.18* |
| G1 | *14.23* | *9.06* |
| G2 | *4.64* | *7.13* |
| F1 | *9.07* | *10.20* |
| F2 | *8.78* | *9.50* |
| F3 | *5.00* | *7.48* |
| E1 | *8.51* | *8.38* |
| E3 | *5.43* | *7.70* |

Figure 4.9 shows the peak pressure at each sensor as a percentage of the G1 value. Looking at the intersection between pillars G and F, the data shows a 16% drop in pressure between G1 and Base1. This is identical to the drop seen between these two sensors in the Around Pillar test. Similarly, the 62% and 33% pressure readings at F2 and G2 are very close to the 63% and 39% recordings in the Around Pillar test. These results show that wave propagation at this three-way type intersection can be consistent between different tunnel configurations.

The second thing to look at here is the difference in the pressures down the center and upper drift. There is a significant difference in the pressures at analogous locations in each drift such as Base1:Base4, Base2:Base5, and Base3:Base6. For each pair, the sensor located in the upper drift measured a pressure that is at least 40% lower than in the center

drift, with the most drastic difference being at Base4 which is 52% smaller than the pressure reading at sensor Base1.

Lastly, there is an interesting contrast between this split test and the Around Pillar set-up at the Base7 sensor. While the pressure in the center drift is lower in both designs, the pressure at Base7 for the split test is 39% of the G1 pressure, matching the results from the Straight-line control tests (Section 4.1.1). This is twice the 19% pressure in the Around Pillar test. It appears that the energy that has been split between the two drifts manages to converge at the exit and provide a pressure that is equivalent to what would have been experienced if the wave traveled down only one drift.

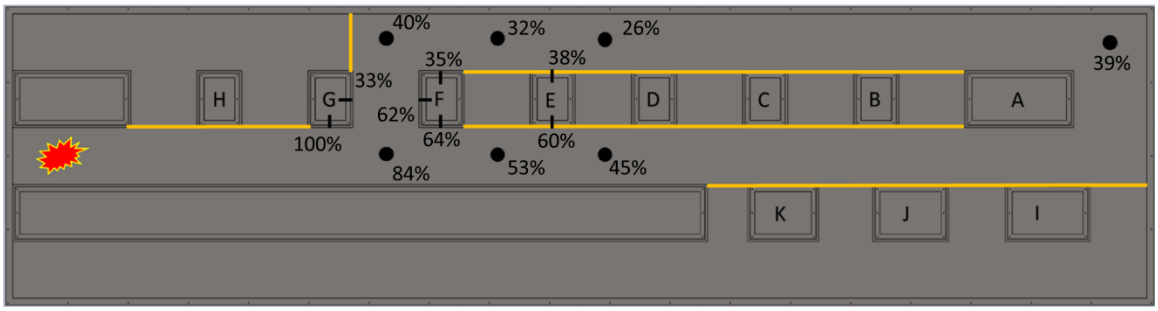


Figure 4.9: Split Peak Pressures with respect to Sensor G1

Looking at Figure 4.10, the data once again shows that the maximum impulse does not decrease as quickly across the model as the peak pressure. Even at the exit sensor, Base7, the impulse is still at 79% of the G1 value. Like the pressure readings, the maximum impulses between the drift pairs (Base1:Base4, etc.) are smaller for the upper drift, but this difference is only by a maximum of 22% as opposed to the 40% to 60% seen with the pressure.

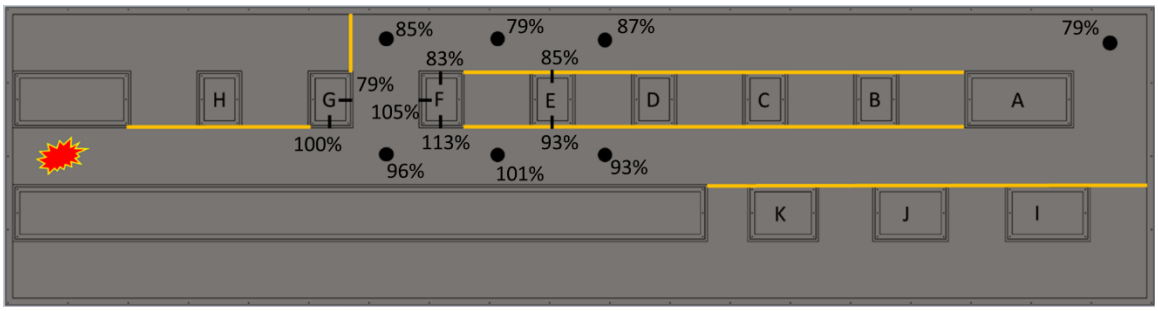


Figure 4.10: Split Maximum Impulses with respect to Sensor G1

**4.1.5. Split Around Pillar.** The last scenario tested for this thesis was the Split Around Pillar tunnel design. This set-up essentially combines the Around Pillar and Split designs discussed above (Sections 4.1.3 and 4.1.4). A blasting cap is detonated at the left end of the center drift, then the crosscut between pillars G and F connects the center drift to the upper drift. Then, there is a second connection between the two drifts between pillars F and E, creating a scenario with a channel all the way around Pillar F, and two drifts that lead all the way the portal at sensor Base7. Figure 3.10 shows the diagram for this model set-up. This test design uses sixteen PCB sensors to record pressure throughout the model, and the peak pressures and maximum impulses determined from this data are shown below in Table 4.5.

This test scenario brought forth some insightful results, showing that the pressures experienced in the crosscuts are very similar between each of our different intersection scenarios. Additionally, this test shows that even with the full channel around pillar F, the pressure at the Base7 portals sensor is comparable to the Straight-line and Split tests. This gives more credence to the earlier assertion that the route around pillar F, in the Around Pillar tests, acted as an energy sink and helped reduce pressures further down the drift.

Table 4.5: Split Around Pillar Average Peak Pressure and Average Maximum Impulse

| Sensor | Peak Pressure (psi) | Maximum Impulse (psi*ms) |
|---|---|---|
| BASE1 | *11.91* | *9.00* |
| BASE2 | *7.38* | *9.54* |
| BASE3 | *5.49* | *9.13* |
| BASE4 | *5.80* | *8.45* |
| BASE5 | *5.27* | *8.49* |
| BASE6 | *4.53* | *8.71* |
| BASE7 | *5.48* | *6.61* |
| G1 | *13.93* | *9.54* |
| G2 | *5.17* | *7.54* |
| F1 | *9.58* | *10.55* |
| F2 | *9.14* | *10.16* |
| F3 | *5.78* | *8.82* |
| F4 | *4.76* | *8.70* |
| E1 | *7.77* | *9.08* |
| E2 | *6.46* | *8.33* |
| E3 | *4.83* | *6.39* |

Looking first at the peak pressures with respect to sensor G1, shown in Figure 4.11, the data shows that the pressure at the Base1 sensor in the GF crosscut and center drift intersection is 85% of the G1 value. This is nearly equal to the 84% value recorded at the Base1 sensor in both the Around Pillar and Split test scenarios discussed previously. Additionally, the 66% and 37% pressure values at the F2 and G2 sensors are very close to the F2 and G2 values found in the Around Pillar and Split tests.

Moving to the FE crosscut, the data again shows similarities between the Split Around Pillar and the Around Pillar scenarios. In fact, the 53%, 46%, and 34% pressure values with respect to sensor G1, at sensors Base2, E2, and F4 respectively, are exactly the same in both of these tests. This, combined with the consistent pressures measured in the first crosscut between pillars G and F, show that reliable pressure ratios can be found

between the sensor closest to the blast, and those located at intersections further away from detonation.

Another thing to look at with this Split Around Pillar tunnel design is the 39% peak pressure value at the Base7 sensor, immediately before the exit of the model. This 39% is the same pressure ratio seen in the Split test, and only slightly higher than the 38% pressure at this sensor in the Straight-line control scenario. However, the 39% exit pressure is double what was experienced in the Around Pillar tunnel with a 19% pressure value at the Base7 sensor. The difference between each of these scenarios is whether or not the upper drift continues all the way to the exit. In the Split and Split Around Pillar tests, every pathway leads to the exit, resulting in a pressure ratio that is very close to that seen in the control set-up. In the Around Pillar test, the upper drift ends in a corner and is redirected back to the center drift. This resulted in blast energy being trapped in the channel around pillar F, leading to lower pressures down the rest of the drift, and especially at the Base7 portal sensor.

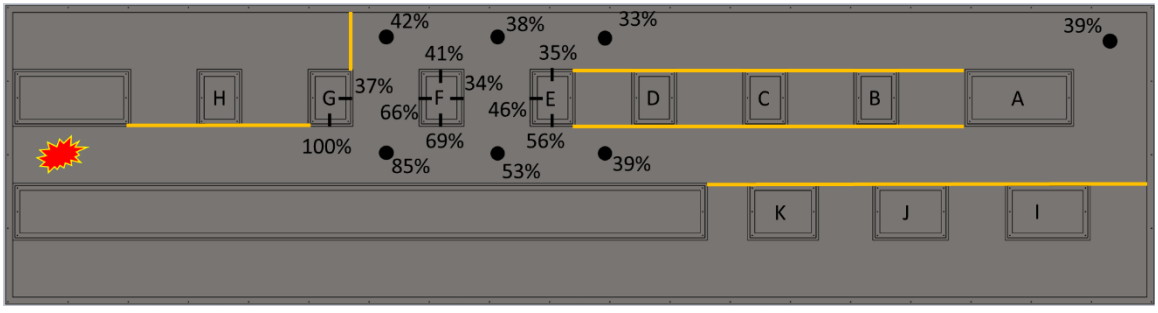


Figure 4.11: Split Around Pillar Peak Pressures with respect to Sensor G1

Once again, the maximum impulse ratio between the G1 and the rest of the pressure sensors does not change as drastically down the length of the model as the pressure values. In this Split Around Pillar scenario, impulse stays at 89% or higher for all but two of the sensors, G2 and Base7. The maximum impulse at G2 is 79% of the G1 value, which is still much higher than the 37% pressure percentage experienced at the same sensor. Similarly, the 69% maximum impulse recorded at Base7 is 1.77 times larger than its 39% peak pressure ratio. As with the previous scenarios, these high impulse percentages are a result of the many reflections caused by the walls and pillars in the model and the channeling effect that the enclosed tunnel creates. These reflections produce positive pressures for a longer period of time which leads to the consistently high impulse.

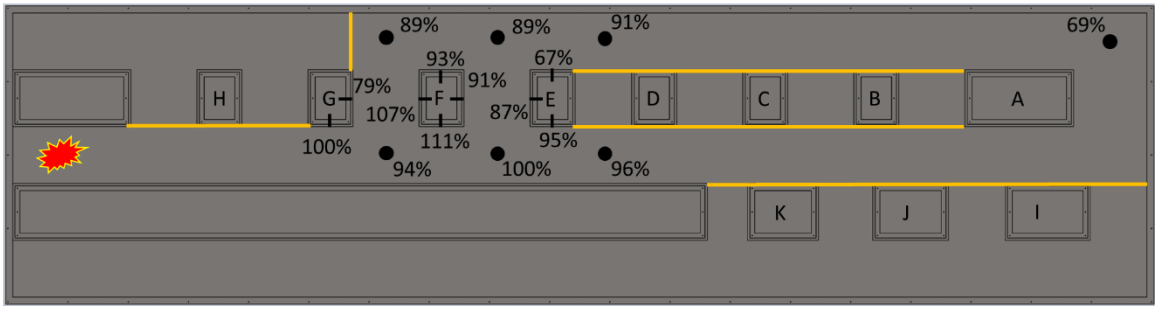


Figure 4.12: Split Around Pillar Maximum Impulses with respect to Sensor G1

## 4.2. BLAST WAVE PROPERTIES AT TUNNEL EXIT

The previous discussions in Section 4 have shown how the shock wave created by the blasting cap propagates through each of the five model designs introduced in Section 3.3. This section will look more specifically at how the wave degraded between the first sensor, G1, and the Base7 sensor located just before the exit of the model. One question

that must be asked in an experiment like this is whether the different tunnel features are causing the changes in pressure and impulse at the tunnel exit, or is it just an artifact from increasing the volume of the system when changing the pathway? The following analysis will show that tunnel characteristics play the dominant role in this testing.

To begin, Table 4.6 and Table 4.7 show the change in average peak pressure and average maximum impulse between sensors G1 and Base7 for all five tunnel designs. These tables also show the pathway volume for each scenario, and the designs are listed left to right from lowest to highest volume.

Table 4.6: Peak Pressure Change from G1 to Base7

| Average Peak Pressure (psi) | | | | | |
|---|---|---|---|---|---|
| **Design** | **One Turn** | **Straight-line** | **Around Pillar** | **Split Test** | **Split Around Pillar** |
| **G1** | 12.80 | 13.76 | 14.70 | 14.23 | 13.93 |
| **BASE7** | 6.46 | 5.16 | 2.84 | 5.56 | 5.48 |
| **BASE7/G1 %** | 50% | 38% | 19% | 39% | 39% |
| **Volume ($ft^3$)** | 21.75 | 21.99 | 26.11 | 35.51 | 36.68 |

Table 4.7: Maximum Impulse Change from G1 to Base7

| Average Max Impulse (psi*ms) | | | | | |
|---|---|---|---|---|---|
| **Design** | **One Turn** | **Straight-line** | **Around Pillar** | **Split Test** | **Split Around Pillar** |
| **G1** | 11.63 | 13.29 | 11.96 | 9.06 | 9.54 |
| **BASE7** | 8.10 | 7.01 | 5.00 | 7.18 | 6.61 |
| **Base7/G1 %** | 70% | 53% | 42% | 79% | 69% |
| **Volume ($ft^3$)** | 21.75 | 21.99 | 26.11 | 35.51 | 36.68 |

The data from these tables is arranged in Figure 4.13, which plots the average peak pressure and maximum impulse at Base7 for each tunnel design versus the volume of the system. From this figure it becomes clear that any effect volume has is overshadowed by

the changing characteristics of the pathway. Between the One Turn and Straight-line models there is a steep drop in both pressure and impulse, followed by another decrease from the Around Pillar tunnel. Then, there is a large increase in volume between the Around Pillar and the Split scenarios which is accompanied by a pressure and impulse increase. From the Split to the Split Around Pillar designs there is a small increase in volume and a slight decrease in pressure and impulse. This data does not reflect the indirect relationship between pressure and volume that would be expected without the effects of the crosscuts and intersections in the model. Once again, the data shows how the channel around Pillar F in the Around Pillar tests caused the greatest pressure decrease at the model exit.

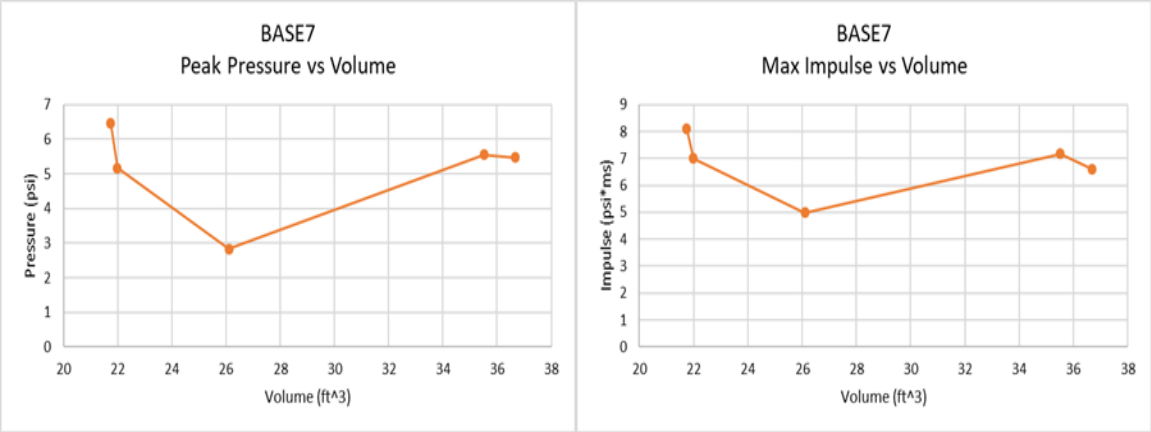


Figure 4.13: Peak Pressure and Maximum Impulse vs Volume for Base7 Sensor

Along with the data from Table 4.6 and Figure 4.13, the pressure traces from the tests help to provide a more thorough picture of how the blast wave changed from G1 closest to the charge to Base7 at the portal. To begin, Figure 4.14 shows a pressure trace at sensor G1 from the Straight-line test, and Figure 4.15 shows a pressure trace at sensor

Base7 from the same test. Both figures have a Friedlander waveform superimposed on top of the empirical data. This Friedlander curve models a typical free field shock wave based on three measured values, namely peak pressure, time of arrival, and positive phase duration. Figure 4.14 shows a strong correlation between the Friedlander model and the empirical data recorded by the PCB pressure sensor at G1, particularly in the initial positive phase. However, Figure 4.15 shows just how much the pressure wave has changed between G1 and Base7, looking much different than just a lower peak pressure. The thing that stands out when comparing the pressure trace for Base7 with its corresponding Friedlander model is the large rise time captured by the PCB sensors. Rise time is the difference in time between the beginning of the positive phase and the time of peak pressure. Rise times for a shock wave are usually very small, and in fact, the Friedlander model discussed in Section 2.2 just assumes the rise time of the pressure curve to be zero seconds. In real-world testing, the jump in pressure associated with the shock cannot truly happen instantaneously, but is still impressively sudden, on the order of $10^{-5}$ seconds at the G1 sensor in these scale model tests.

The average rise times at G1 and Base7 for each scenario are shown in Table 4.8. Looking at the bottom row of this table, the data shows that the One Turn test has the smallest Base7 to G1 rise time ratio, and the Base7 rise time is still almost 18 times longer than the rise time at G1. This shows that the many reflections occurring within the model, as well as the distance traveled by the wave, deteriorate the shock front and create a more gently rising pressure wave.

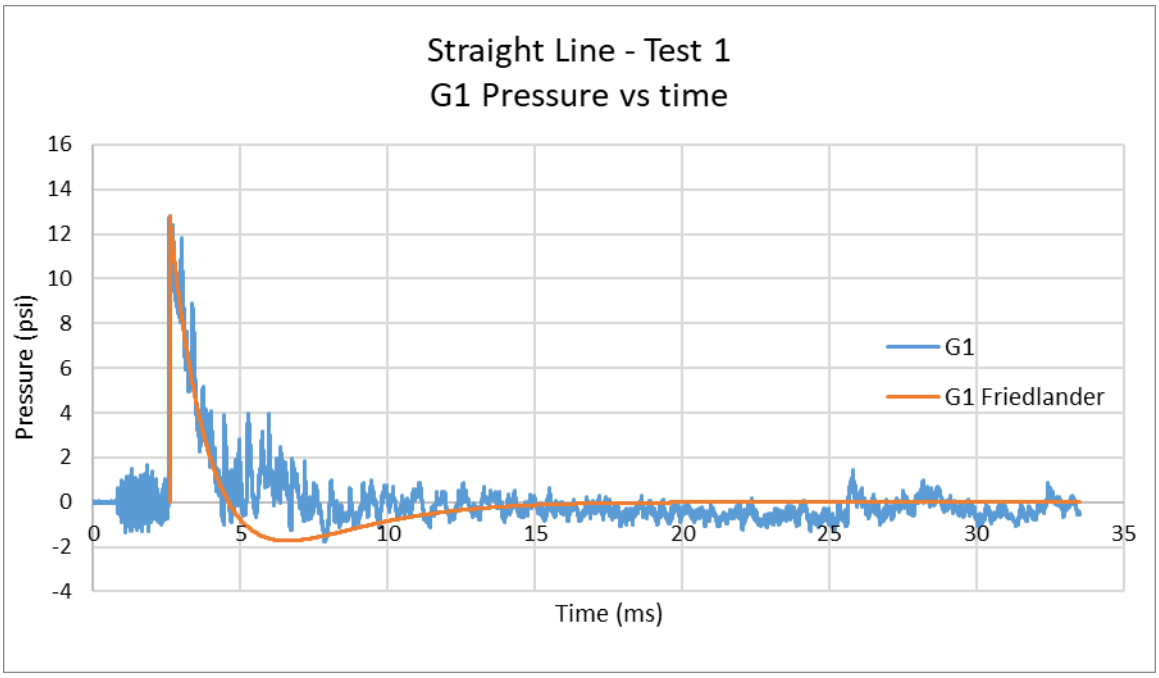


Figure 4.14: Straight-line Sensor G1 Pressure Curve with Friedlander Overlay

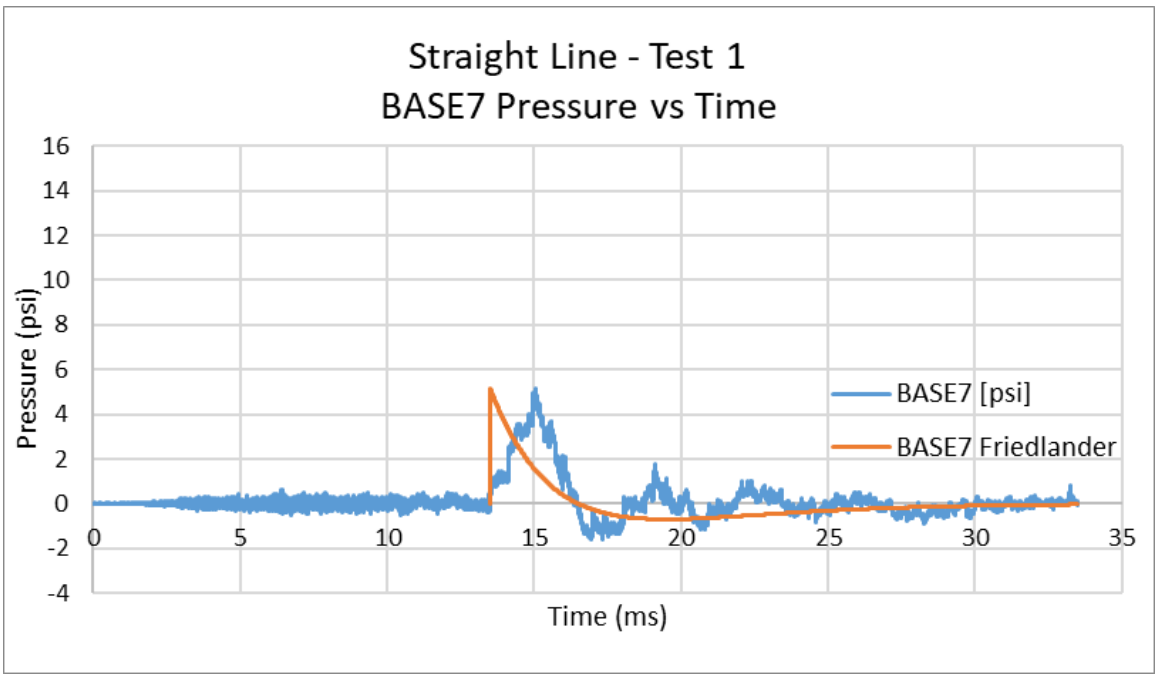


Figure 4.15: Straight-line Sensor Base7 Pressure Curve with Friedlander Overlay

Table 4.8: Sensor G1 and Base7 Average Rise Times

| Average Rise Time (ms) | | | | | |
|---|---|---|---|---|---|
| **Design** | **Straight-line** | **One Turn** | **Around Pillar** | **Split Test** | **Split Around Pillar** |
| **G1** | 0.06 | 0.07 | 0.02 | 0.05 | 0.04 |
| **BASE7** | 1.52 | 1.16 | 1.58 | 1.51 | 1.06 |
| **BASE7/G1** | 27.02 | 17.87 | 68.87 | 30.81 | 23.66 |

A representative pressure trace of sensors G1 and Base7 is shown below for one test of each of the four remaining tunnel designs. Looking at the G1 traces, there are some slight differences in peak pressure between the scenarios, but the general shape of the waveform remained consistent throughout the testing, except for the Single Turn tunnel design. The waveform shape for the Base7 pressure curves are more varied, but all have a rise time that is much longer than expected of a shock wave.

Unlike the other G1 pressure traces, the pressure recording at G1 for the Single Turn design (Figure 4.17) shows a substantial second peak occurring after the initial shock has already passed and the conditions have reached ambient pressure. Looking at the diagram in Figure 3.7, it becomes clear that the second peak is a reflection off of the stopping across the center drift at Pillar F, shown in yellow. Similarly, the Base7 graph for the Single Turn test shows a double peak, although the pressure does not return to ambient levels between peaks at this sensor. This second peak at the portal sensor is caused by the pressure wave's orientation with the portal as it exits the model. Figure 4.16 shows how the model exit is not facing the same direction as the pressure wave is traveling down the drift. This causes the wave to reflect off of the outside wall of the model and travel back towards the Base7 sensor, resulting in the twin peaked pressure trace seen in Figure 4.17.

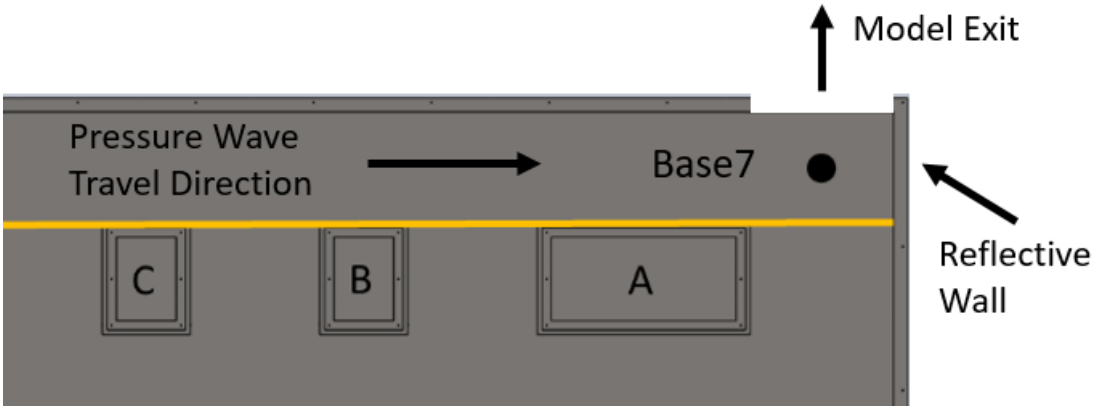


Figure 4.16: Single Turn Portal Orientation

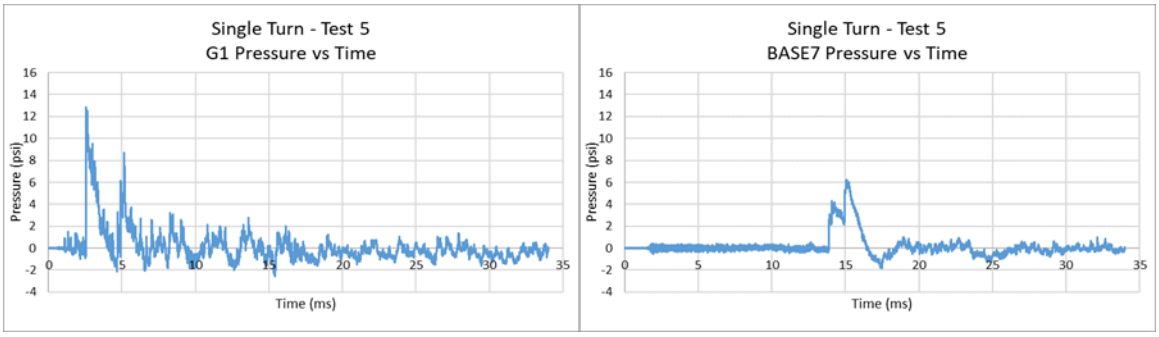


Figure 4.17: Single Turn Pressure Traces for Sensors G1 and Base7

The Base7 pressure trace for the Around Pillar tests shown in Figure 4.19 looks very much like a scaled down version of the Straight-line Base7 results (Figure 4.15). This is likely because both scenarios have all the pressure coming from the center drift immediately before the portal, as shown in Figure 4.18. This pressure curve further validates the idea that the channel around pillar F in the Around Pillar design traps a good portion of the blast energy from the detonator and significantly reduces pressures further down the drift.

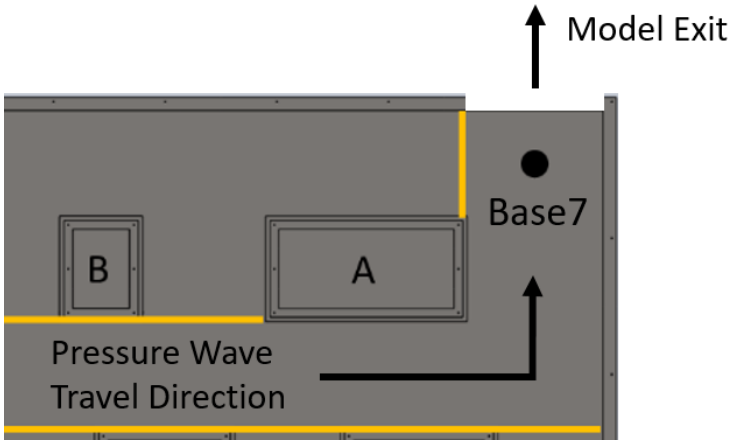


Figure 4.18: Straight-line and Around Pillar Portal Orientation

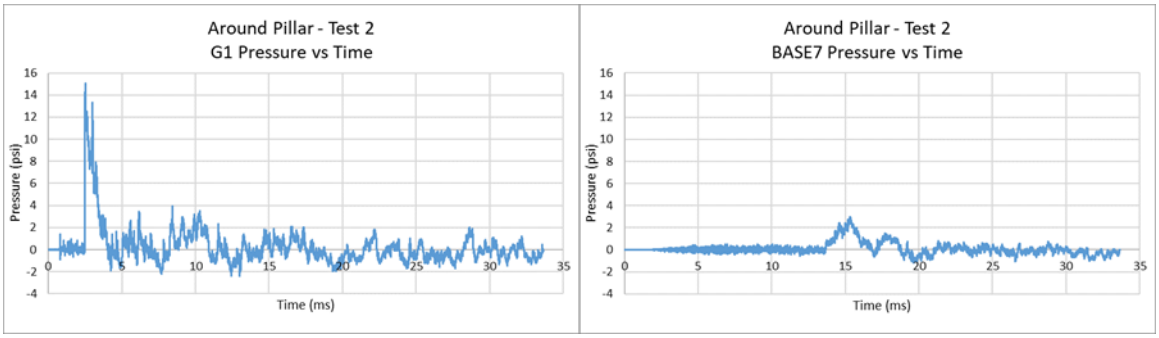


Figure 4.19: Around Pillar Pressure Traces for Sensors G1 and Base7

The Base7 traces for the Split and Split Around Pillar tests in Figure 4.21 and Figure 4.22 are similar to the pressure curve for the Straight-line test, but have a bit of a plateau across the top. This is more pronounced in the Split Around Pillar data than in the Split test. Again, this slight form variation is likely due to how the pressure wave approaches the Base7 sensor at the model exit, shown in Figure 4.21. In these two scenarios, the blast wave is split between the top and center drifts, resulting in two waves converging on the Base7 sensor at approximately the same time. These converging waves and the slight time

difference between their arrivals result in the prolonged high-pressure period experienced in these tests.

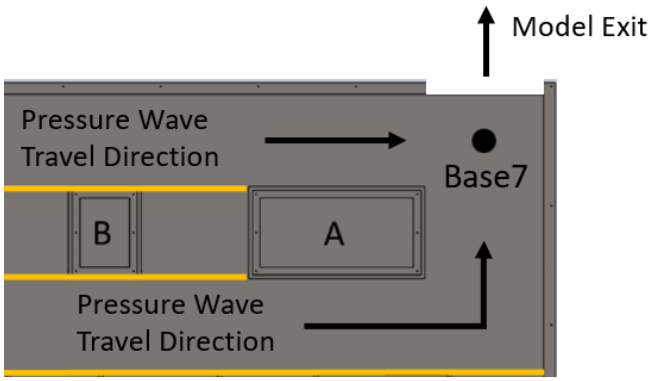


Figure 4.20: Split and Split Around Pillar Portal Orientation

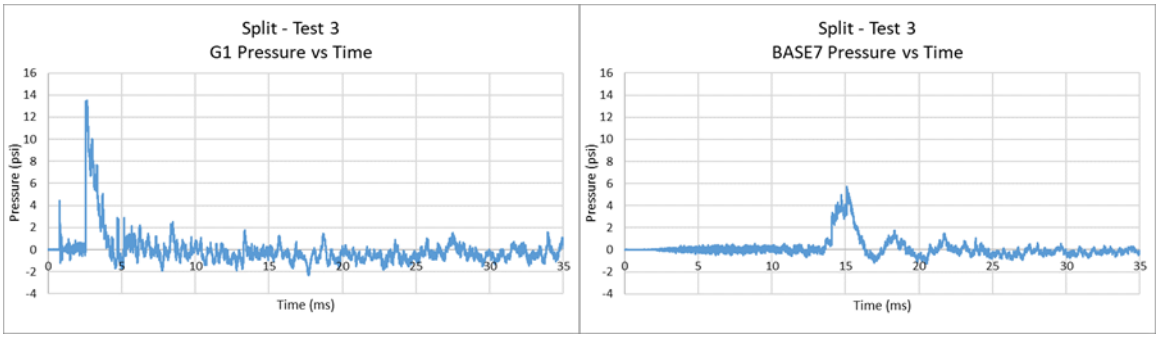


Figure 4.21: Split Pressure Traces for Sensors G1 and Base7

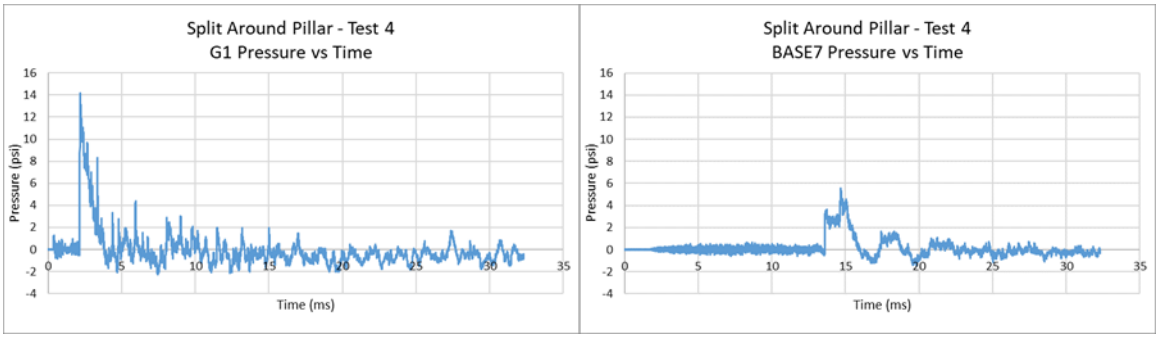


Figure 4.22: Split Around Pillar Pressure Traces for Sensors G1 and Base7

## 4.3. ANALYSIS SUMMARY

Straight-line – This tunnel is a simple straight-line with a ninety degree turn at the model exit. This design acts as a control for the remaining four pathways. As is the case with all of the tunnel designs, pressure and impulse were found at various locations in the mine model. This data was presented by showing pressure and impulse values as a percentage of the G1 sensor values, which was closest to the blast. In this scenario, the pressure and impulse at the exit were 38% and 53% of their respective G1 values.

Single Turn – This scenario had a single crosscut connecting the center and upper drifts of the model. The intersections between the drifts and crosscuts were forced corners, such that all of the product gases followed the same two-corner path. The most noticeable finding from this tunnel design was the pressure values at G2 and F2, the sensors in the crosscut. These sensors had very similar readings for both pressure and impulse, showing that in a forced corner the near and far wall of a crosscut will receive similar blast loading. The pressure and impulse readings at the portal for this test were 50% and 70% of the corresponding G1 values.

Around Pillar – The third design tested had a channel around Pillar F that reconnects to the middle drift and does not continue down the top drift. This test provided one of the most interesting results with the Base7 portal sensor only receiving 19% of the G1 pressure and 42% of the G1 impulse. This was the lowest portal pressure of any of the test scenarios. It appears that the channel around Pillar F trapped and dissipated a good portion of the blast energy, decreasing the pressure and impulse readings further down the drift.

Split – The Split design connects the middle and upper drifts with a crosscut between Pillars G and F, and both drifts continue to the portal. The data from the crosscut in this test showed good consistency with the GF crosscut in the Around Pillar tests. This begins to show that pressure and impulse data at open intersections will remain consistent even if the downstream is varied. Additionally, the 39% and 79% pressure and impulse values at Base7 are very similar to the same sensor readings from the Straight-line control test.

Split Around Pillar – This final tunnel design combines the Around Pillar and Split scenarios with a channel all the way around Pillar F, but in the Split Around Pillar scenario, the upper drift continues all the way to the portal Comparing crosscut pressure values between the Split Around Pillar, Around Pillar, and Split tests show that the analogous crosscuts receive similar blast loading in all three tests. This further validates the claim from the Split test analysis that intersection values are predictable between different tunnel designs, and not greatly affected by downstream conditions. The Base7 exit values for the Split Around Pillar scenario are 39% and 69% of the pressure and impulse G1 values. This helps to confirm the idea in the Around Pillar analysis that the closed channel around Pillar F, meaning the top pathway does not continue all the way to the model exit, contributed to the lower pressures further down the drift. The Split Around Pillar tunnel has the same channel around Pillar F, but it is open to the portal through the upper drift. This opening allows energy to continue to travel down the model and converge at the portal sensor.

# 5. CONCLUSION

Shock wave interactions in closed environments are more complicated and less understood than those occurring from open air or surface detonations. However, there are many circumstances, both intentional and accidental, where explosives are used in enclosed spaces, so work must be done to better understand these scenarios. Coal dust explosions and urban bombings are both tragedies involving confined explosive events that result in the loss of innocent life. Explosive breaching is a useful tool available to law enforcement and military personnel to force entry when needed, but when done improperly can cause lasting damage to those completing the task. An improved understanding of shock wave behavior in enclosed spaces can help ensure the safety of miners, soldiers, and the public.

This thesis tested five unique tunnel scenarios to observe how a shock wave propagates through different pathways with various corners and intersections. The six trials in each of the Straight-line, Single Turn, Around Pillar, Split, and Split Around Pillar designs yielded statistically repeatable results. The data analysis in this thesis discovered high- and low-pressure locations in each of the tunnel scenarios and found locations that experienced similar shock interaction across multiple designs.

The following list of conclusions drawn from this thesis can be taken into consideration to improve mine safety, urban blast mitigation, and explosive breacher long-term health.

- At a forced corner, the pressures experienced at the near and far walls of the crosscut will be nearly identical.

  - In the Single Turn tests (Section 4.1.2) the pressures at the G2 and F2 sensors, located on the near and far walls of the intersecting pathway respectively were nearly identical at 78% and 79% of the G1 pressure. This tunnel set-up forced all blast energy through this turn, unlike the other scenarios where the center pathway is open until the exit. In the other scenarios, Pillar G creates a partially shielded area such that sensor G2 on the close wall experiences much lower pressures than sensor F2 on the opposing wall. This phenomenon is replicated with maximum impulse as well.

- Circulating channel around pillar acts as an energy sink, greatly reducing pressure further down the drift and at the portal.
  - The Around Pillar testing (Section 4.1.3) showed that the sections of the tunnel downstream of Pillar E experienced significantly lower pressure and impulse than in the other test scenarios. It appears that the pathway around Pillar F, which reconnects to the center hallway and does not continue to the model exit, traps and dissipates a large portion of the explosive energy. This is reflected in the impulse data which shows very high impulse values at all sensors surrounding Pillar F.
- Crosscuts at an intersection see significant differences between the near and far walls.
  - Unlike the results from the Single Turn test, sensors G2 and F2 experienced very different peak pressure and maximum impulse levels in the Around Pillar, Split, and Split Around Pillar tunnels (Sections 4.1.3-4.1.5) In these

designs the center drift continues past the intersecting crosscut. This means some of the blast energy continued forward and some diffracted into the connecting path. The diffraction mechanics lead to greater pressure and impulse at the opposing wall (F2) and lower pressure and impulse on the near wall of the crosscut (G2)

- Tunnel volume does not have a significant effect on the pressure and impulse values experienced at the tunnel exit.
    - A comparison between tunnel volume and the shock wave characteristics recorded at the tunnel exit (sensor Base7) show that volume and pressure do not have the indirect relationship that would be expected from an open-air blast scenario. The data presented in Section 4.2 shows the lowest pressure and impulse at Base7 were both observed during the Around Pillar test, which is not the test with the highest volume. In fact, the pressure and impulse values for the Straight-line, Split, and Split Around Pillar tests are all very similar, even though they vary in volume by more than 14 cubic feet.

# 6. FUTURE WORKS

This study uncovered some interesting patterns involving tunnel characteristics and shock wave propagation. Hopefully, the patterns that seem the most promising for improving safety, like the drastic decrease in pressure after the channel around Pillar F in the Around Pillar scenario testing (Section 4.1.3), can be further investigated so a better understanding of the mechanism behind this phenomenon can be found. Additionally, the modularity of the model used in the testing for this thesis will allow for continued testing of different tunnel designs. Specifically, more work should be done investigating dead ends that cause a split in the propagating shock wave close to the point of detonation, but do not provide a path all the way to the portal. These features should act similarly to the Pillar F channel in the Around Pillar testing, trapping and dissipating the explosive energy before it can propagate further down the mine, causing more damage and potential loss of life.

Something else that the model can accommodate is shock wave studies that are more specifically tailored for studying urban bombings. Remove the polycarbonate roof, and the model is perfect for testing blast behavior in high building density urban settings. Taking things a step further, new structures can be fabricated and bolted into the existing base. This opens the opportunity for modeling buildings of different heights, unlike the uniform height of the current pillars, or even creating uniquely shaped structures if scale model testing on a specific building or landscape is desired.

Another area of future testing would be to place multiple sensors at different locations on the same pillar face. This would provide more detailed information on the low- and high-pressure areas discovered from this testing. To supplement this higher

fidelity measured data, computer modelling of the model systems can be completed using ANSYS or other software. The information generated from the computer modelling can be compared to the recorded test results to verify the accuracy of the computer model, and the computer model can be used to discover new information about the system that may be missed due to the limit on how many sensors can be physically placed in the model.

# APPENDIX A.

# PRESSURE AND IMPULSE DATA

## STRAIGHT-LINE

Table A.1: Straight-line Peak Pressures

| Peak Pressure (psi) | | | | | | | | | |
|---|---|---|---|---|---|---|---|---|---|
| **Sensor** | **Test1** | **Test2** | **Test3** | **Test4** | **Test5** | **Test6** | **Mean** | **Standard Deviation** | **95% Confidence Interval** |
| **BASE1** | 15.15 | 15.87 | 15.16 | 15.99 | 14.30 | 14.22 | ***15.12*** | 0.75 | ± 0.79 |
| **BASE2** | 9.51 | 10.44 | 10.00 | 9.74 | 10.26 | 9.95 | ***9.98*** | 0.34 | ± 0.35 |
| **BASE3** | 8.79 | 8.09 | 8.42 | 8.20 | 8.48 | 8.53 | ***8.42*** | 0.25 | ± 0.26 |
| **BASE7** | 5.17 | 5.00 | 5.05 | 5.28 | 5.14 | 5.33 | ***5.16*** | 0.13 | ± 0.13 |
| **G1** | 12.83 | 13.92 | 14.14 | 14.00 | 14.33 | 13.34 | ***13.76*** | 0.56 | ± 0.59 |
| **F1** | 10.91 | 11.65 | 12.31 | 11.32 | 12.24 | 10.75 | ***11.53*** | 0.66 | ± 0.69 |
| **E1** | 9.67 | 9.59 | 9.70 | 9.20 | 9.49 | 9.52 | ***9.53*** | 0.18 | ± 0.19 |

Table A.2: Straight-line Maximum Impulses

| Maximum Impulse (ms*psi) | | | | | | | | | |
|---|---|---|---|---|---|---|---|---|---|
| **Sensor** | **Test1** | **Test2** | **Test3** | **Test4** | **Test5** | **Test6** | **Mean** | **Standard Deviation** | **95% Confidence Interval** |
| **BASE1** | 12.72 | 12.77 | 13.44 | 13.34 | 13.40 | 12.69 | ***13.06*** | 0.37 | ± 0.38 |
| **BASE2** | 12.27 | 12.93 | 13.10 | 13.26 | 13.32 | 12.89 | ***12.96*** | 0.38 | ± 0.40 |
| **BASE3** | 10.67 | 11.00 | 11.29 | 11.40 | 11.59 | 11.19 | ***11.19*** | 0.32 | ± 0.34 |
| **BASE7** | 6.88 | 6.85 | 7.07 | 7.04 | 7.17 | 7.07 | ***7.01*** | 0.12 | ± 0.13 |
| **G1** | 12.54 | 13.23 | 13.46 | 13.61 | 13.61 | 13.27 | ***13.29*** | 0.40 | ± 0.42 |
| **F1** | 12.11 | 12.76 | 12.97 | 13.19 | 13.06 | 12.73 | ***12.80*** | 0.38 | ± 0.40 |
| **E1** | 11.16 | 11.60 | 11.84 | 12.00 | 12.01 | 11.80 | ***11.73*** | 0.32 | ± 0.34 |

## SINGLE TURN

The hyphens in the tables for sensors F2 and F3 indicate a recording with an unusually high level of noise or other anomalies that indicated the data may not be representative. In these cases, no value was provided for these sensors, and that was

considered when calculating the statistics for the sensor (i.e. sensor F2 calculations were treated as if there were only four trials completed, and F3 as if there were only three).

Table A.3: Single Turn Peak Pressures

| Peak Pressure (psi) | | | | | | | | | |
|---|---|---|---|---|---|---|---|---|---|
| **Sensor** | **Test1** | **Test2** | **Test3** | **Test4** | **Test5** | **Test6** | **Mean** | **Standard Deviation** | **95% Confidence Interval** |
| **BASE1** | 15.15 | 14.45 | 14.87 | 13.47 | 14.93 | 13.20 | ***14.34*** | 0.82 | ± 0.86 |
| **BASE4** | 8.18 | 9.04 | 8.61 | 8.46 | 8.88 | 9.34 | ***8.75*** | 0.42 | ± 0.44 |
| **BASE5** | 5.97 | 6.33 | 6.32 | 6.35 | 5.70 | 6.28 | ***6.16*** | 0.27 | ± 0.28 |
| **BASE6** | 6.51 | 6.28 | 6.46 | 6.07 | 5.99 | 6.16 | ***6.24*** | 0.21 | ± 0.22 |
| **BASE7** | 6.65 | 6.51 | 6.36 | 6.51 | 6.23 | 6.47 | ***6.46*** | 0.14 | ± 0.15 |
| **G1** | 13.51 | 12.80 | 12.04 | 13.90 | 12.84 | 11.73 | ***12.80*** | 0.83 | ± 0.87 |
| **G2** | 9.48 | 10.22 | 10.56 | 9.66 | 10.17 | 10.18 | ***10.04*** | 0.40 | ± 0.42 |
| **F2** | 10.92 | - | - | 9.50 | 10.52 | 9.34 | ***10.07*** | 0.77 | ± 1.23 |
| **F3** | - | - | - | 8.96 | 8.72 | 8.63 | ***8.77*** | 0.17 | ± 0.42 |
| **E3** | 8.37 | 8.82 | 8.15 | 8.04 | 8.31 | 7.82 | ***8.25*** | 0.34 | ± 0.36 |

Table A.4: Single Turn Maximum Impulses

| Maximum Impulse (psi*ms) | | | | | | | | | |
|---|---|---|---|---|---|---|---|---|---|
| **Sensor** | **Test1** | **Test2** | **Test3** | **Test4** | **Test5** | **Test6** | **Mean** | **Standard Deviation** | **95% Confidence Interval** |
| **BASE1** | 12.07 | 11.74 | 11.84 | 11.99 | 11.86 | 11.76 | ***11.88*** | 0.13 | ± 0.14 |
| **BASE4** | 11.49 | 11.15 | 11.33 | 11.29 | 11.07 | 10.99 | ***11.22*** | 0.18 | ± 0.19 |
| **BASE5** | 9.90 | 10.04 | 10.13 | 9.94 | 10.11 | 10.12 | ***10.04*** | 0.10 | ± 0.10 |
| **BASE6** | 10.21 | 10.06 | 9.97 | 9.92 | 9.78 | 9.81 | ***9.96*** | 0.16 | ± 0.17 |
| **BASE7** | 8.21 | 8.13 | 8.07 | 8.04 | 8.10 | 8.06 | ***8.10*** | 0.06 | ± 0.07 |
| **G1** | 12.06 | 11.85 | 11.18 | 11.72 | 11.53 | 11.42 | ***11.63*** | 0.32 | ± 0.33 |
| **G2** | 12.00 | 11.75 | 11.98 | 11.75 | 11.58 | 11.51 | ***11.76*** | 0.20 | ± 0.21 |
| **F2** | 11.10 | - | - | 10.47 | 10.45 | 10.48 | ***10.63*** | 0.32 | ± 0.50 |
| **F3** | - | - | - | 10.47 | 10.45 | 10.48 | ***10.47*** | 0.01 | ± 0.04 |
| **E3** | 10.34 | 9.92 | 10.15 | 10.13 | 10.11 | 10.06 | ***10.12*** | 0.14 | ± 0.14 |

**AROUND PILLAR**

Table A.5: Around Pillar Peak Pressures

| Peak Pressure (psi) | | | | | | | | | |
|---|---|---|---|---|---|---|---|---|---|
| **Sensor** | **Test1** | **Test2** | **Test3** | **Test4** | **Test5** | **Test6** | **Mean** | **Standard Deviation** | **95% Conf. Interval** |
| **BASE1** | 11.63 | 12.68 | 12.87 | 12.35 | 12.82 | 12.17 | ***12.42*** | 0.47 | ± 0.50 |
| **BASE2** | 7.34 | 7.82 | 8.01 | 8.21 | 7.95 | 7.62 | ***7.82*** | 0.31 | ± 0.32 |
| **BASE3** | 5.14 | 5.23 | 5.24 | 5.35 | 5.51 | 5.42 | ***5.31*** | 0.14 | ± 0.14 |
| **BASE4** | 5.31 | 5.66 | 5.32 | 5.37 | 5.55 | 5.65 | ***5.48*** | 0.16 | ± 0.17 |
| **BASE5** | 7.89 | 7.70 | 7.94 | 7.86 | 7.95 | 8.32 | ***7.94*** | 0.21 | ± 0.22 |
| **BASE7** | 2.81 | 2.98 | 2.81 | 2.65 | 2.72 | 3.04 | ***2.84*** | 0.15 | ± 0.16 |
| **G1** | 14.05 | 15.06 | 14.89 | 15.40 | 14.44 | 14.36 | ***14.70*** | 0.50 | ± 0.53 |
| **G2** | 5.71 | 5.56 | 5.83 | 6.44 | 5.57 | 5.52 | ***5.77*** | 0.35 | ± 0.37 |
| **F1** | 8.81 | 9.12 | 9.44 | - | 8.76 | 9.09 | ***9.04*** | 0.27 | ± 0.34 |
| **F2** | 8.54 | 9.41 | 10.15 | 9.71 | 8.40 | 9.16 | ***9.23*** | 0.68 | ± 0.71 |
| **F3** | 5.64 | 5.79 | 5.78 | 5.95 | 6.34 | 5.35 | ***5.81*** | 0.33 | ± 0.35 |
| **F4** | 4.66 | 5.30 | 4.92 | - | 5.23 | 5.15 | ***5.06*** | 0.26 | ± 0.32 |
| **E1** | 7.77 | 7.62 | 7.69 | 7.86 | 7.91 | 7.76 | ***7.77*** | 0.11 | ± 0.11 |
| **E2** | 6.50 | 7.11 | 6.92 | 6.58 | 6.82 | 6.70 | ***6.77*** | 0.22 | ± 0.23 |

Table A.6: Around Pillar Maximum Impulses

| Maximum Impulse (ms*psi) | | | | | | | | | |
|---|---|---|---|---|---|---|---|---|---|
| **Sensor** | **Test1** | **Test2** | **Test3** | **Test4** | **Test5** | **Test6** | **Mean** | **Standard Deviation** | **95% Conf. Interval** |
| **BASE1** | 11.61 | 12.08 | 11.96 | 11.34 | 11.34 | 10.80 | ***11.52*** | 0.47 | ± 0.49 |
| **BASE2** | 11.53 | 11.94 | 11.54 | 11.36 | 10.95 | 11.33 | ***11.44*** | 0.32 | ± 0.34 |
| **BASE3** | 10.38 | 10.75 | 10.68 | 10.25 | 10.18 | 9.72 | ***10.33*** | 0.37 | ± 0.39 |
| **BASE4** | 10.61 | 10.87 | 10.90 | 10.56 | 10.32 | 9.79 | ***10.51*** | 0.41 | ± 0.43 |
| **BASE5** | 12.39 | 12.96 | 12.80 | 12.64 | 12.10 | 12.12 | ***12.50*** | 0.36 | ± 0.37 |
| **BASE7** | 4.83 | 5.28 | 5.15 | 4.90 | 4.97 | 4.85 | ***5.00*** | 0.18 | ± 0.19 |
| **G1** | 11.50 | 12.89 | 12.50 | 11.38 | 11.98 | 11.49 | ***11.96*** | 0.62 | ± 0.65 |
| **G2** | 9.75 | 10.05 | 10.05 | 9.71 | 9.62 | 9.41 | ***9.76*** | 0.25 | ± 0.26 |
| **F1** | 13.42 | 13.64 | 13.70 | - | 13.05 | 12.64 | ***13.29*** | 0.44 | ± 0.55 |
| **F2** | 12.82 | 12.94 | 13.10 | 10.71 | 12.24 | 12.35 | ***12.36*** | 0.87 | ± 0.92 |
| **F3** | 11.65 | 12.02 | 12.11 | 10.96 | 11.54 | 10.97 | ***11.54*** | 0.49 | ± 0.52 |
| **F4** | 11.19 | 11.70 | 12.41 | - | 11.66 | 11.43 | ***11.68*** | 0.46 | ± 0.57 |
| **E1** | 11.36 | 11.62 | 11.64 | 11.27 | 11.08 | 10.49 | ***11.25*** | 0.43 | ± 0.45 |
| **E2** | 12.82 | 12.38 | 12.19 | 11.69 | 11.50 | 11.05 | ***11.94*** | 0.65 | ± 0.68 |

**SPLIT**

Table A.7: Split Peak Pressures

| Peak Pressure (psi) | | | | | | | | | |
|---|---|---|---|---|---|---|---|---|---|
| **Sensor** | **Test1** | **Test2** | **Test3** | **Test4** | **Test5** | **Test6** | **Mean** | **Standard Deviation** | **95% Conf. Interval** |
| **BASE1** | 11.95 | 12.92 | 11.92 | 11.46 | 11.20 | 11.95 | ***11.90*** | 0.59 | ± 0.62 |
| **BASE2** | 7.83 | 7.71 | 7.66 | 7.42 | 7.27 | 7.27 | ***7.53*** | 0.24 | ± 0.25 |
| **BASE3** | 6.20 | 6.63 | 6.43 | 6.59 | 6.44 | 6.45 | ***6.46*** | 0.15 | ± 0.16 |
| **BASE4** | 5.85 | 5.61 | 5.93 | 6.00 | 5.35 | 5.47 | ***5.70*** | 0.26 | ± 0.28 |
| **BASE5** | 4.49 | 4.62 | 4.77 | 4.47 | 4.27 | 4.97 | ***4.60*** | 0.25 | ± 0.26 |
| **BASE6** | 3.88 | 3.80 | 3.80 | 3.67 | 3.74 | 3.71 | ***3.77*** | 0.08 | ± 0.08 |
| **BASE7** | 5.72 | 5.67 | 5.73 | 5.55 | 5.28 | 5.41 | ***5.56*** | 0.18 | ± 0.19 |
| **G1** | - | 14.01 | 13.54 | 14.91 | 14.53 | 14.16 | ***14.23*** | 0.52 | ± 0.65 |
| **G2** | 4.67 | 5.32 | 4.44 | 4.81 | 4.32 | 4.27 | ***4.64*** | 0.39 | ± 0.41 |
| **F1** | - | 9.31 | 8.81 | 9.42 | 8.87 | 8.92 | ***9.07*** | 0.28 | ± 0.34 |
| **F2** | - | 8.96 | 8.58 | 8.44 | 9.06 | 8.85 | ***8.78*** | 0.26 | ± 0.32 |
| **F3** | - | 5.14 | 5.00 | 5.15 | 4.76 | 4.94 | ***5.00*** | 0.16 | ± 0.20 |
| **E1** | 9.34 | 8.01 | 8.72 | 8.69 | 7.90 | 8.41 | ***8.51*** | 0.53 | ± 0.56 |
| **E3** | 5.67 | 5.66 | 5.71 | 5.20 | 5.12 | 5.24 | ***5.43*** | 0.27 | ± 0.29 |

Table A.8: Split Maximum Impulses

| Maximum Impulse (ms*psi) | | | | | | | | | |
|---|---|---|---|---|---|---|---|---|---|
| **Sensor** | **Test1** | **Test2** | **Test3** | **Test4** | **Test5** | **Test6** | **Mean** | **Standard Deviation** | **95% Conf. Interval** |
| **BASE1** | 8.57 | 8.55 | 8.75 | 8.81 | 8.53 | 9.13 | ***8.72*** | 0.23 | ± 0.24 |
| **BASE2** | 9.41 | 9.04 | 9.30 | 9.21 | 8.79 | 9.32 | ***9.18*** | 0.23 | ± 0.24 |
| **BASE3** | 8.84 | 8.38 | 8.33 | 8.62 | 8.03 | 8.43 | ***8.44*** | 0.27 | ± 0.29 |
| **BASE4** | 8.00 | 7.53 | 7.66 | 7.84 | 7.36 | 7.68 | ***7.68*** | 0.22 | ± 0.24 |
| **BASE5** | 7.27 | 6.89 | 7.08 | 7.37 | 7.01 | 7.42 | ***7.17*** | 0.21 | ± 0.22 |
| **BASE6** | 8.18 | 7.73 | 7.77 | 8.00 | 7.58 | 7.95 | ***7.87*** | 0.22 | ± 0.23 |
| **BASE7** | 7.47 | 7.20 | 7.19 | 7.27 | 6.90 | 7.04 | ***7.18*** | 0.19 | ± 0.20 |
| **G1** | - | 8.75 | 8.99 | 8.91 | 9.18 | 9.44 | ***9.06*** | 0.26 | ± 0.33 |
| **G2** | 7.16 | 7.01 | 7.22 | 7.22 | 6.92 | 7.24 | ***7.13*** | 0.13 | ± 0.14 |
| **F1** | - | 10.06 | 10.36 | 10.06 | 10.00 | 10.50 | ***10.20*** | 0.22 | ± 0.27 |
| **F2** | - | 9.25 | 9.66 | 9.51 | 9.35 | 9.71 | ***9.50*** | 0.20 | ± 0.25 |
| **F3** | - | 7.38 | 7.53 | 7.67 | 7.24 | 7.59 | ***7.48*** | 0.17 | ± 0.21 |
| **E1** | 8.81 | 8.31 | 8.23 | 8.59 | 7.96 | 8.41 | ***8.38*** | 0.29 | ± 0.31 |
| **E3** | 7.99 | 7.57 | 7.63 | 7.87 | 7.38 | 7.76 | ***7.70*** | 0.22 | ± 0.23 |

**SPLIT AROUND PILLAR**

Table A.9: Split Around Pillar Peak Pressures

| Peak Pressure (psi) | | | | | | | | | |
|---|---|---|---|---|---|---|---|---|---|
| **Sensor** | **Test1** | **Test2** | **Test3** | **Test4** | **Test5** | **Test6** | **Mean** | **Standard Deviation** | **95% Confidence Interval** |
| **BASE1** | 11.61 | 11.57 | 12.87 | 11.99 | 11.41 | 12.02 | ***11.91*** | 0.53 | ± 0.56 |
| **BASE2** | 7.63 | 7.59 | 7.54 | 7.54 | 7.08 | 6.88 | ***7.38*** | 0.31 | ± 0.33 |
| **BASE3** | 5.55 | 5.77 | 5.73 | 5.37 | 5.14 | 5.35 | ***5.49*** | 0.24 | ± 0.25 |
| **BASE4** | 6.21 | 6.14 | 6.02 | 5.36 | 5.43 | 5.67 | ***5.80*** | 0.37 | ± 0.39 |
| **BASE5** | 5.37 | 5.08 | 5.59 | 5.15 | 5.13 | 5.29 | ***5.27*** | 0.19 | ± 0.20 |
| **BASE6** | 4.67 | 4.60 | 4.63 | 4.54 | 4.33 | 4.41 | ***4.53*** | 0.14 | ± 0.14 |
| **BASE7** | 5.63 | 5.42 | 5.67 | 5.54 | 5.37 | 5.26 | ***5.48*** | 0.16 | ± 0.17 |
| **G1** | 14.46 | 13.64 | 14.69 | 14.18 | 13.73 | 12.90 | ***13.93*** | 0.65 | ± 0.68 |
| **G2** | 6.07 | 5.03 | 5.21 | 4.74 | 4.49 | 5.51 | ***5.17*** | 0.56 | ± 0.59 |
| **F1** | 10.28 | 9.52 | 9.81 | 9.29 | 9.55 | 9.04 | ***9.58*** | 0.43 | ± 0.45 |
| **F2** | 9.58 | 9.14 | 9.19 | 9.01 | 8.96 | 8.94 | ***9.14*** | 0.24 | ± 0.25 |
| **F3** | 5.80 | 6.04 | 5.80 | 5.74 | 5.55 | 5.73 | ***5.78*** | 0.16 | ± 0.17 |
| **F4** | 5.15 | 4.73 | 4.91 | 4.69 | 4.64 | 4.43 | ***4.76*** | 0.25 | ± 0.26 |
| **E1** | 7.94 | 7.80 | 8.26 | 7.64 | 7.38 | 7.61 | ***7.77*** | 0.31 | ± 0.32 |
| **E2** | 6.60 | 6.52 | 6.69 | 6.38 | 6.16 | 6.42 | ***6.46*** | 0.19 | ± 0.20 |
| **E3** | 5.26 | 4.86 | 5.21 | 4.60 | 4.41 | 4.65 | ***4.83*** | 0.34 | ± 0.36 |

Table A.10: Split Around Pillar Maximum Impulses

| Maximum Impulse (ms*psi) | | | | | | | | | |
|---|---|---|---|---|---|---|---|---|---|
| **Sensor** | **Test1** | **Test2** | **Test3** | **Test4** | **Test5** | **Test6** | **Mean** | **Standard Deviation** | **95% Confidence Interval** |
| **BASE1** | 8.86 | 9.46 | 8.82 | 9.28 | 8.53 | 9.03 | ***9.00*** | 0.34 | ± 0.35 |
| **BASE2** | 9.35 | 9.70 | 9.97 | 9.83 | 8.78 | 9.62 | ***9.54*** | 0.43 | ± 0.45 |
| **BASE3** | 9.69 | 9.35 | 9.17 | 9.06 | 8.42 | 9.10 | ***9.13*** | 0.42 | ± 0.44 |
| **BASE4** | 8.96 | 8.58 | 8.41 | 8.44 | 7.82 | 8.46 | ***8.45*** | 0.37 | ± 0.39 |
| **BASE5** | 8.88 | 8.49 | 8.52 | 8.58 | 8.00 | 8.47 | ***8.49*** | 0.28 | ± 0.30 |
| **BASE6** | 9.23 | 8.91 | 8.71 | 8.65 | 8.08 | 8.70 | ***8.71*** | 0.38 | ± 0.40 |
| **BASE7** | 6.95 | 6.77 | 6.80 | 6.54 | 6.11 | 6.50 | ***6.61*** | 0.30 | ± 0.31 |
| **G1** | 11.58 | 9.53 | 9.58 | 8.73 | 8.61 | 9.18 | ***9.54*** | 1.08 | ± 1.13 |
| **G2** | 7.90 | 7.65 | 7.52 | 7.66 | 6.99 | 7.54 | ***7.54*** | 0.30 | ± 0.32 |
| **F1** | 11.03 | 10.86 | 10.44 | 10.96 | 9.66 | 10.33 | ***10.55*** | 0.52 | ± 0.54 |
| **F2** | 10.67 | 10.37 | 10.16 | 10.36 | 9.45 | 9.94 | ***10.16*** | 0.43 | ± 0.45 |
| **F3** | 9.32 | 8.94 | 8.91 | 8.83 | 8.15 | 8.79 | ***8.82*** | 0.38 | ± 0.40 |
| **F4** | 9.19 | 8.65 | 8.76 | 8.79 | 8.02 | 8.77 | ***8.70*** | 0.38 | ± 0.40 |
| **E1** | 9.59 | 9.30 | 9.10 | 9.03 | 8.38 | 9.06 | ***9.08*** | 0.40 | ± 0.42 |
| **E2** | 7.93 | 9.22 | 8.40 | 7.93 | 8.28 | 8.25 | ***8.33*** | 0.47 | ± 0.50 |
| **E3** | 7.48 | 6.92 | 5.53 | 5.50 | 6.36 | 6.54 | ***6.39*** | 0.78 | ± 0.81 |

# APPENDIX B.

# PRESSURE VS TIME GRAPHS

This appendix contains the pressure vs time graphs for every sensor in each of the five tunnel designs tested in this thesis. One representative trial for each tunnel was chosen for this appendix.

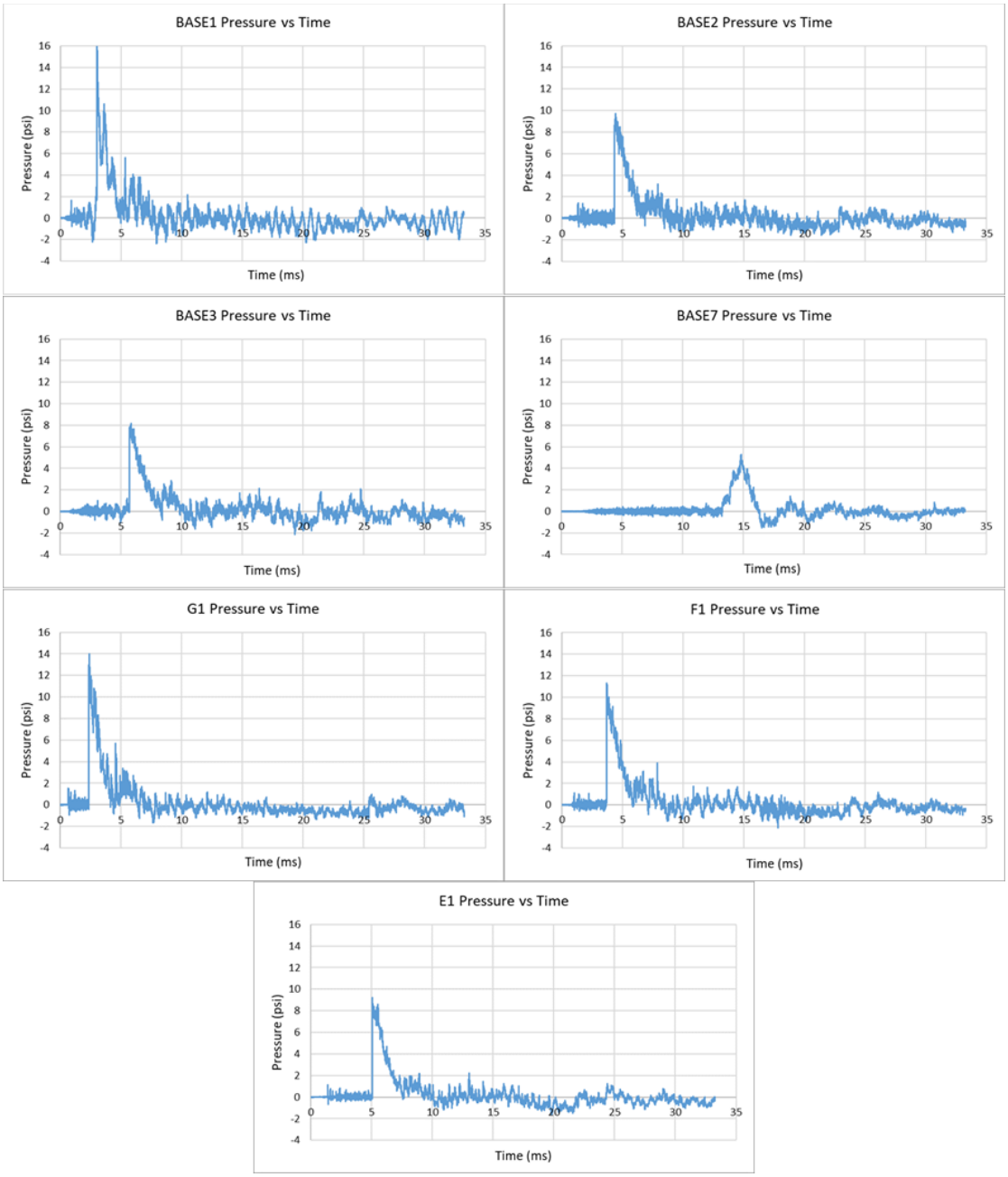


Figure B.1: Straight Line Pressure Waveforms (Test 4)

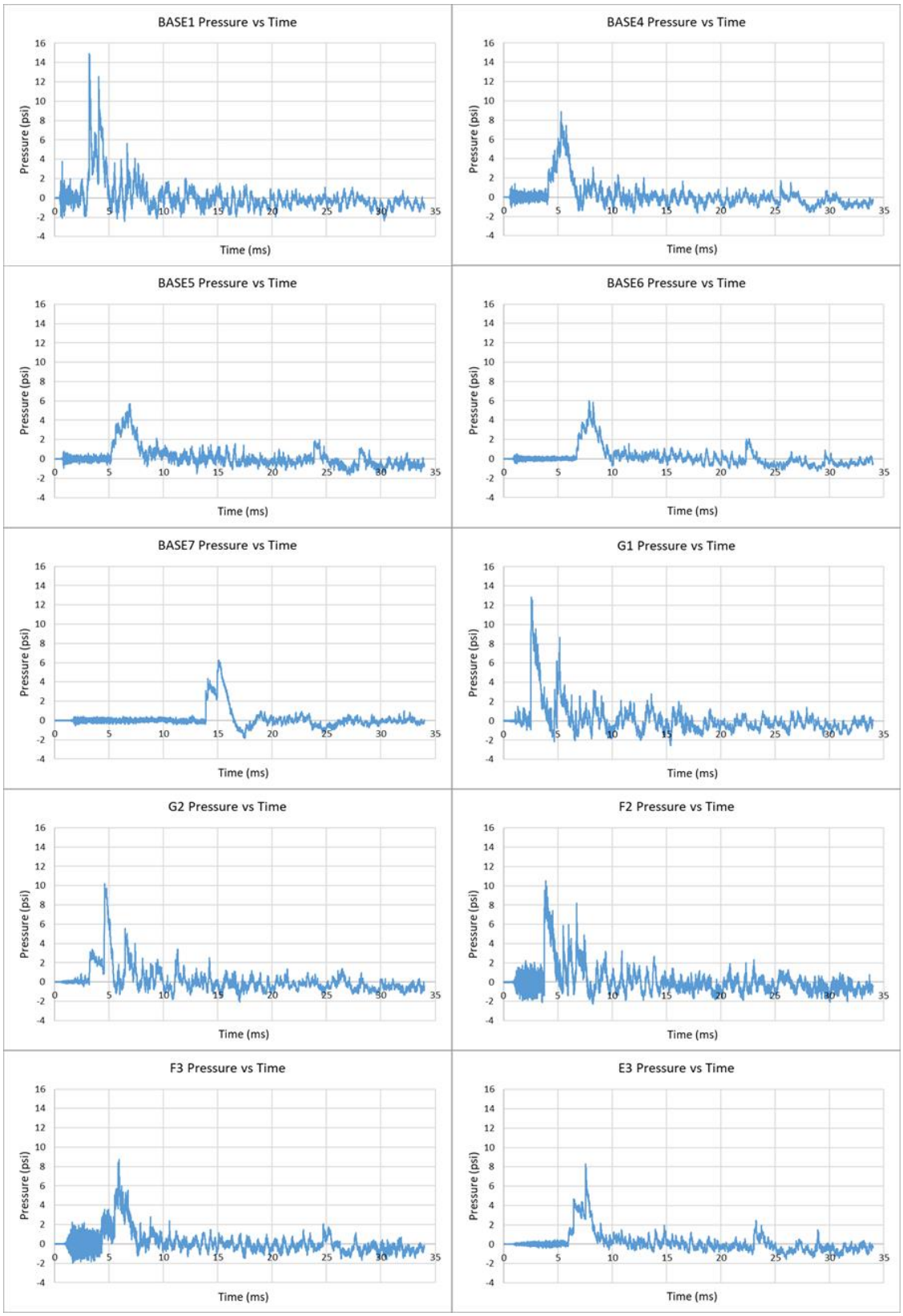


Figure B.2: Single Turn Pressure Waveforms (Test 5)

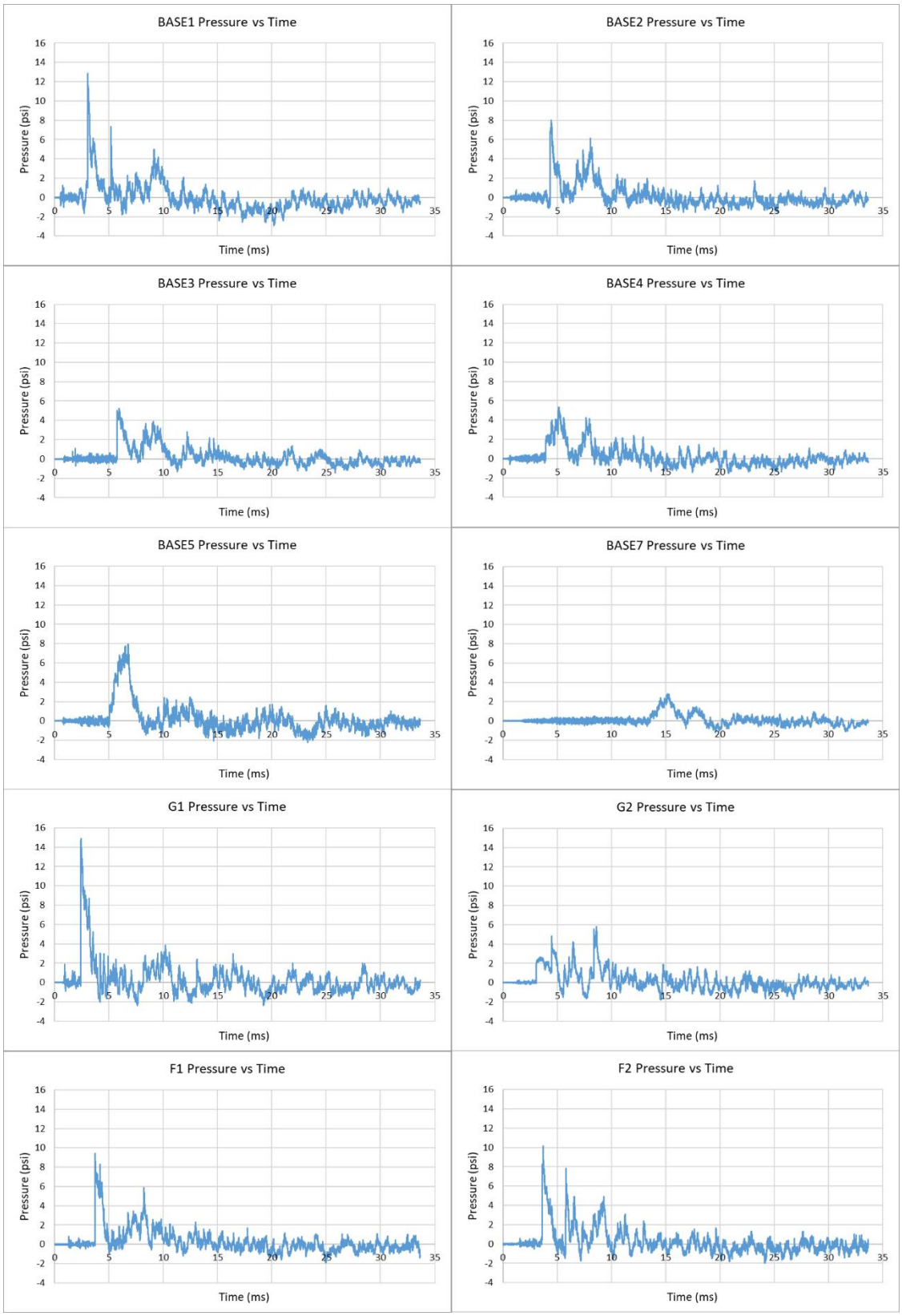


Figure B.3: Around Pillar Pressure Waveforms (Test 3)

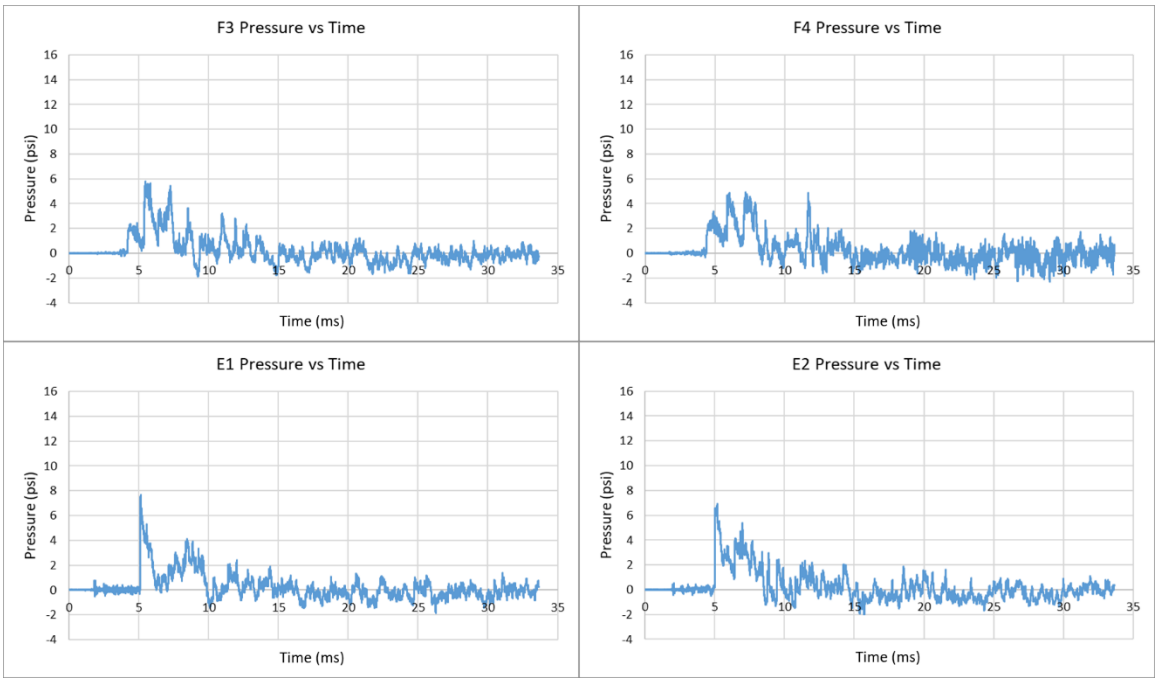


Figure B.3: Around Pillar Pressure Waveforms (Test 3) (Cont.)

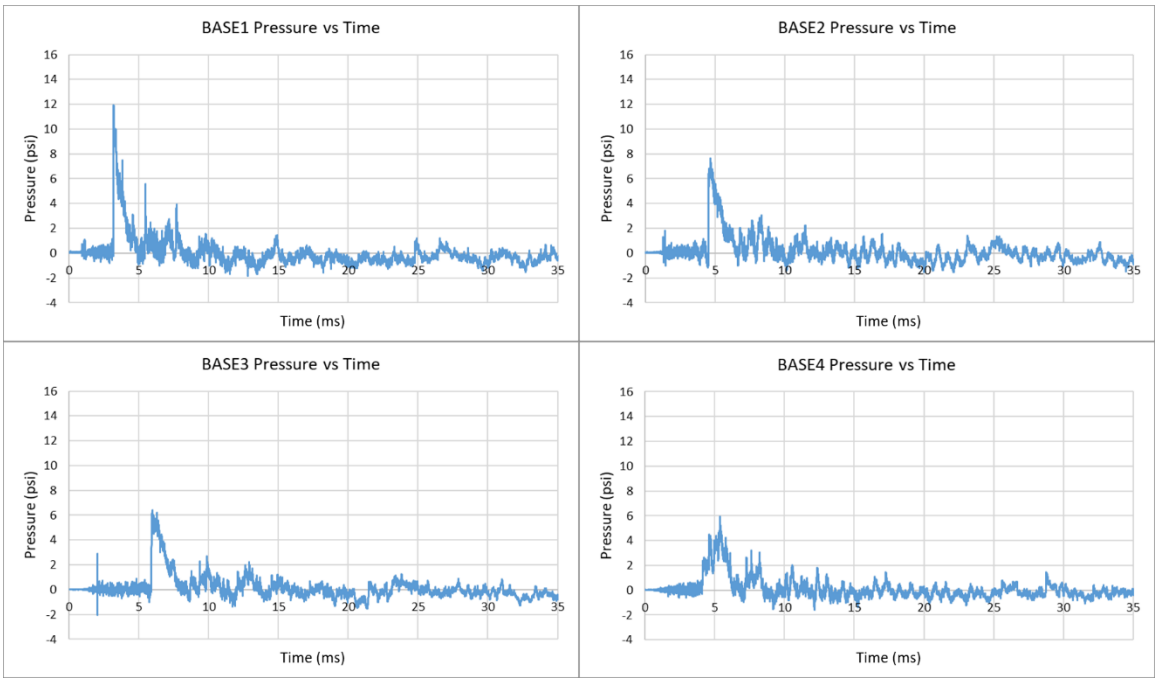


Figure B.4: Split Test Pressure Waveforms (Test 3)

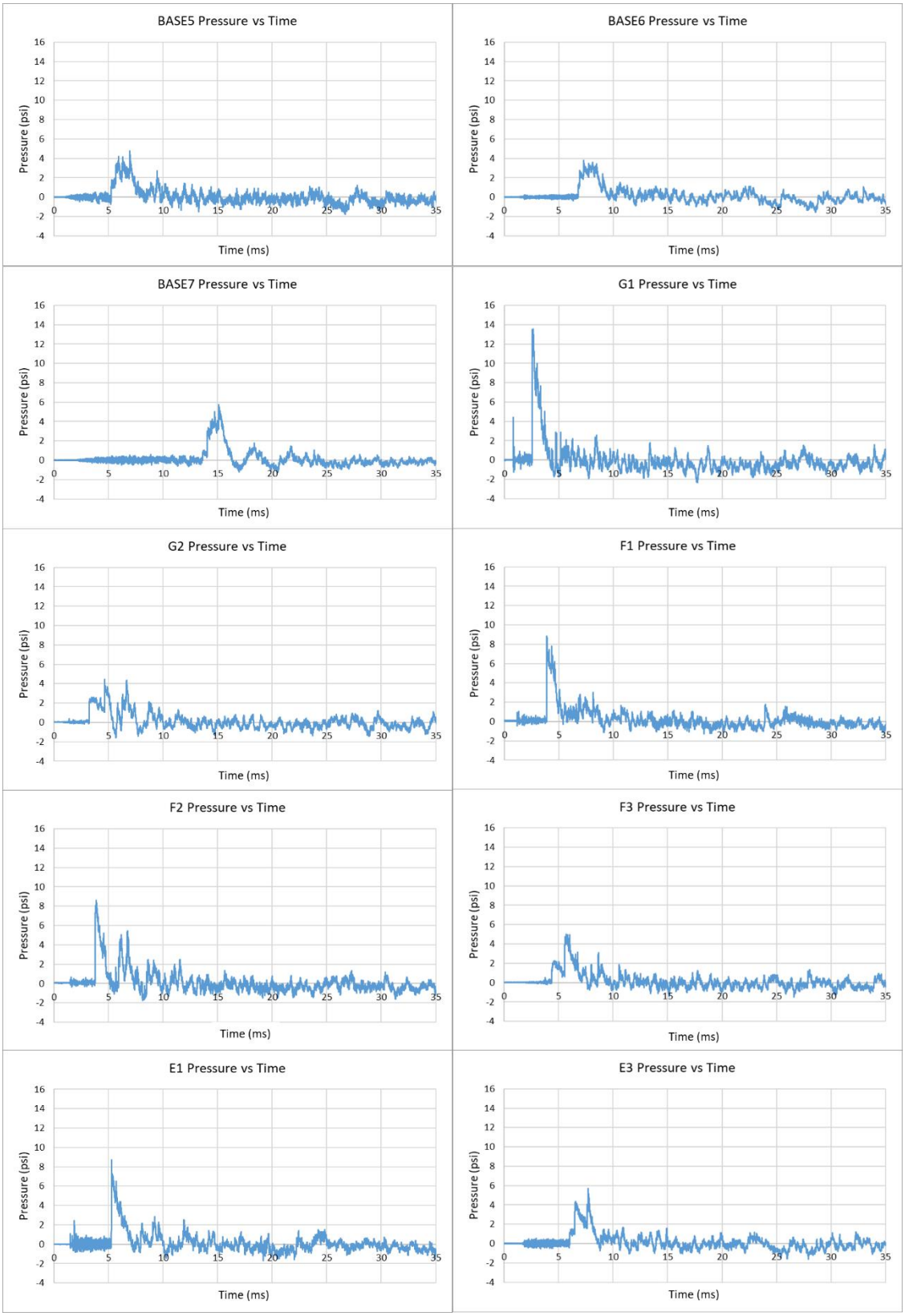


Figure B.4: Split Test Pressure Waveforms (Test 3) (Cont.)

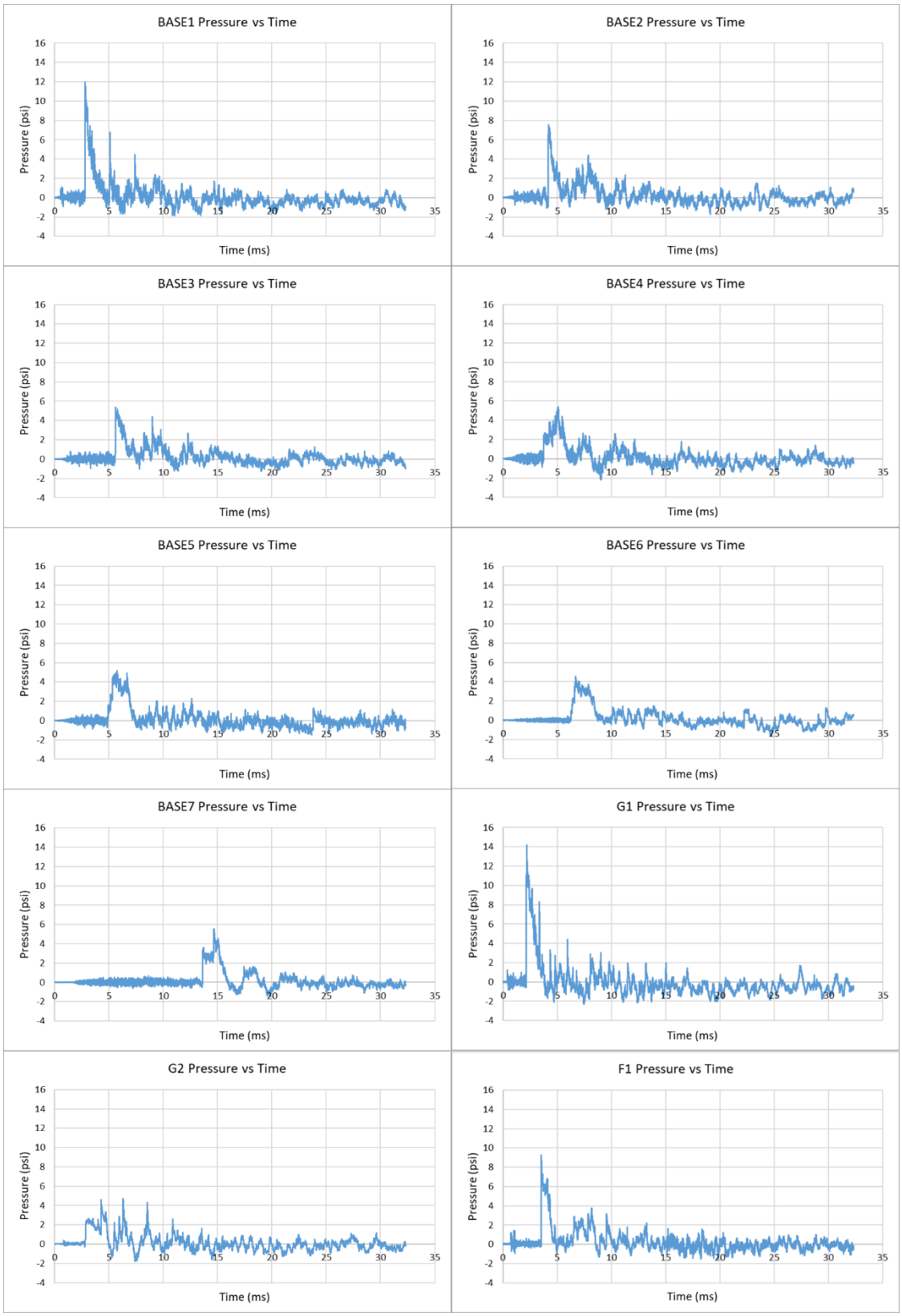


Figure B.5: Split Around Pillar Pressure Waveforms (Test 4)

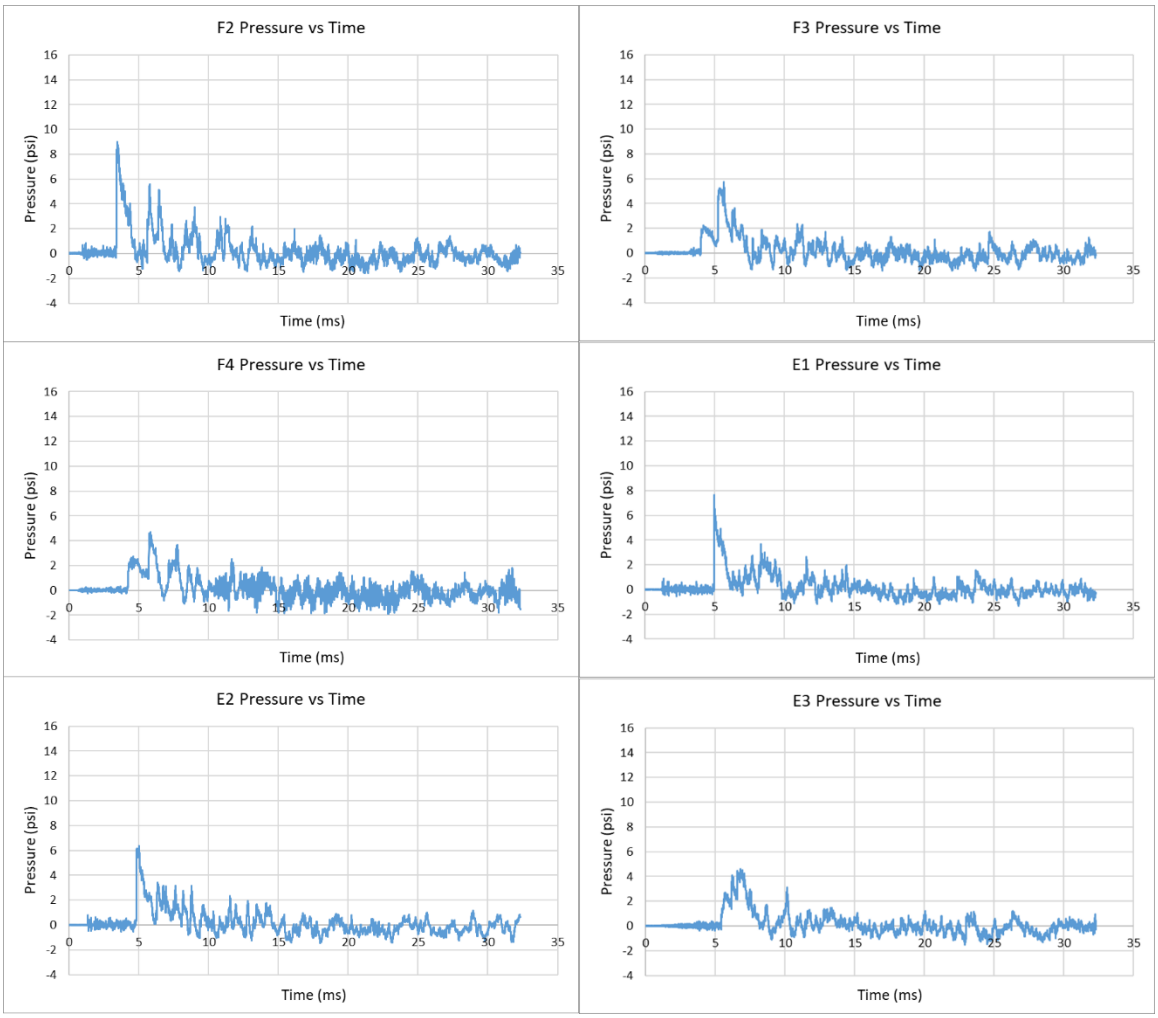


Figure B.5: Split Around Pillar Pressure Waveforms (Test 4) (Cont.)

# APPENDIX C.

# IMPEDANCE AND SHOCK REFLECTION

When a shock travelling through one medium impacts a new medium, the impedance difference between the two mediums will determine how much energy is reflected back into the first medium, and whether the pressure reflection will be positive or negative. This relationship is described in Equation (C1) [70]. In this equation $P_r$ is reflected pressure, $P_i$ is incident pressure, $Z_1$ is the impedance of the initial medium, and $Z_2$ is the impedance of the impacted medium. Impedance is calculated using the density ($\rho$) of and speed of sound ($v_a$) in a material, as shown in Equation (C2) [71]. From analyzing Equation (C1) it can be deduced that the greater the difference between $Z_2$ and $Z_1$ the larger the magnitude of the reflected pressure, and that when $Z_2 > Z_1$ the sign will be positive, but when $Z_2 < Z_1$ the sign will be negative.

$$\frac{P_r}{P_i} = \frac{Z_2 - Z_1}{Z_2 + Z_1} \tag{C1}$$

$$Z = \rho * v_a \tag{C2}$$

For example, air, quartz, and steel have impedance values of $0.4 \times 10^3$, $1.5 \times 10^7$, and $4.7 \times 10^7$ respectively, so a shock moving from air to steel or air to rock would have a positive reflection, and a shock moving from steel or rock into air would have a negative reflection [71]. Also, because the difference in impedance between these solid mediums and air is so much greater than the difference between the steel and the quartz, the magnitude of the reflection from air to either steel or rock (quartz) will be nearly the same in both cases. With air and steel $P_r / P_i = 0.99998$ and with air and quartz, $P_r / P_i = 0.99995$.

# REFERENCES


[1] J. R. Schafler, "Management of coal dust explosions in United States' coal mines using bag type passive explosion barriers"," 2018. [Online]. Available: https://scholarsmine.mst.edu/masters_theses/7782. [Accessed 23 November 2019].

[2] Federal Bureau of Investigation, "FBI 100 First Strike: Global Terror in America," Federal Bureau of Investigation, 26 February 2008. [Online]. Available: https://archives.fbi.gov/archives/news/stories/2008/february/tradebom_022608. [Accessed 29 January 2020].

[3] Federal Bureau of Investigation, "Oklahoma City Bombing," Federal Bureau of Investigation, [Online]. Available: https://www.fbi.gov/history/famous-cases/oklahoma-city-bombing. [Accessed 29 January 2020].

[4] Ada Derana, "Attacks carried out by suicide bombers, Govt. Analyst confirms," 22 April 2019. [Online]. Available: http://www.adaderana.lk/news/54531/attacks-carried-out-by-suicide-bombers-govt-analyst-confirms. [Accessed 29 January 2020].

[5] E. R. Peskind, E. C. Petrie, D. J. Cross, K. Pagulayan, K. McCraw, D. Hoff, K. Hart, C.-E. Yu, M. A. Raskind, D. G. Cook and S. Minoshima, "Cerebrocerebellar hypometabolism associated with repetitive blast exposure milde traumatic brain injury in 12 Iraq war Veterans with persistant post-concussive symptoms," *NeuroImage*, vol. 54, no. 1, pp. S76-S82, 2011.

[6] N. G. Johnson, "Explosive (Chemical Product)," 6 November 2019. [Online]. Available: https://www.britannica.com/technology/explosive.

[7] "Deflagration," Lexico, [Online]. Available: https://www.lexico.com/en/definition/deflagration. [Accessed 7 November 2019].

[8] "Detonation," Lexico, [Online]. Available: https://www.lexico.com/en/definition/detonation. [Accessed 7 November 2019].

[9] X. Zhang, Z. Chen and Y. Liu, "Governing Equations," in *The Material Point Method*, Academic Press, 2017, pp. 11-36.

[10] M. Attisano, E. Marasca and I. Siciliano, "Chemical Explosives," University of Turin, 2009. [Online]. Available: http://lem.ch.unito.it/didattica/infochimica/2008_Esplosivi/Home.html. [Accessed 7 November 2019].

[11] Military Factory, "explosive train Definition (US DoD)," 2020. [Online]. Available: https://www.militaryfactory.com/dictionary/military-terms-defined.asp?term_id=1986. [Accessed 8 February 2020].

[12] M. S. Macias, "The Development of an Optimized System of Narcotic and Explosive Contraband Mimics for Calibration and Training of Biological Detectors," Florida International University, Miami, 2009.

[13] Dyno Nobel, "Cast Boosters," 2013. [Online]. Available: https://www.dynonobel.com/practical-innovations/popular-products/cast-boosters. [Accessed 8 February 2020].

[14] "Brisance," Merriam-Webster, [Online]. Available: https://www.merriam-webster.com/dictionary/brisance. [Accessed 4 February 2020].

[15] Department of the Army, "Field Manual No. 3-06.11; Ch. 8 - Obstacles, Mines, and Demolitions," 28 February 2002. [Online]. Available: https://www.globalsecurity.org/military/library/policy/army/fm/3-06-11/ch8.htm#par9. [Accessed 5 February 2020].

[16] B. E. Gelfand, M. V. Silnikov, S. P. Medvedev and S. V. Khomik, "Chapter 5: Fast Deflagration and Quasi-Detonation," in *Thermo-Gas Dynamics of Hydrogen Combustion and Explosion*, Berlin Heidelberg, Springer-Verlag, 2012.

[17] B. R. Gardner, R. J. Winter and M. J. Moore, "Explosion development and deflagration-to-detonation transition in coal dust/air suspensions," *Symposium (International) on Combustion*, vol. 21, no. 1, pp. 335-343, 1988.

[18] E. Schultz, E. Wintenberger and J. Shepherd, "Investigation of Deflagration to Detonation Transition for Application to Pulse Detonation Engine Ignition Systems," California Institute of Technology, Pasadena.

[19] "Shock Wave," Lexico, [Online]. Available: https://www.lexico.com/en/definition/shock_wave. [Accessed 21 November 2019].

[20] J. M. Dewey, "The Shape of the Blast Wave: Studies of the Friedlander Equation," in *21st International Symposium on Military Aspects of Blast and Shock*, Israel, 2010.

[21] J. M. Galante, M. J. Martin, C. J. Rodriguez and W. T. Gordon, Managing Dismounted Complex Blast Injuries in Military & Civilian Settings, Springer International Publishing, 2018.

[22] E. G. Morris, "INFLUENCE OF INTERSECTIONS ON BLAST CHANNELING AND DIFFRACTION EFFECTS," University of Kentucky, Lexington, 2012.

[23] P. W. Cooper, "Blast Effects in Air, Water, and on the Human Body," in *Explosives Engineering*, New York, Wiley-VHC, 1996, pp. 405-420.

[24] S. Glasstone and P. J. Dolan, "Air Blast Phenomena in Air and Surface Bursts," in *The Effects of Nuclear Weapons*, Washington D.C., United States Department of Defense and Energy Research and Development Administration, 1977, pp. 80-126.

[25] V. Aune, F. Casadei, G. Valsamos, M. Langseth and T. Borvik, "A Shock Tube Used to Study the Dynamic Response of Blast-Loaded Plates," in *18th International Conference on Experimental Mechanics*, Brussels, 2018.

[26] B. T. Lusk, K. A. Perry and S. P. Lusk, "Predictability of a High Explosives Shock Tube for Testing Blast Resistant Windows," *Blasting and Fragmentation*, vol. 4, no. 2, pp. 75-91, 2010.

[27] J. Hoffman, B. Lusk and K. Perry, "Investigations of Shock Tunnel Dynamics and Energy Realization," *Blasting and Fragmentation*, vol. 3, no. 3, pp. 207-226, 2009.

[28] J. Baird, "Explosive Shocks and Impedance Mismatch in Armatures," *Electromagnetic Phenomena*, vol. 3, no. 3, pp. 405-413, 2003.

[29] P. W. Cooper, "Interaction of Shock Waves," in *Explosives Engineering*, New York, Wiley-VCH, 1996, pp. 203-222.

[30] P. D. Smith and T. A. Rose, "Blast wave propagation in city streets - an overview," *Progress in Structural Engineering and Materials*, vol. 8, pp. 16-28, 2006.

[31] O. Igra, L. Wang, J. Falcovitz and W. Heilig, "Shock wave propagation in a branched duct," *Shock Waves*, vol. 8, pp. 375-381, 1998.

[32] E. G. Morris, "Influence of Intersections on Blast Channeling and Diffraction Effects," University of Kentucky, Lexington, 2012.

[33] H. B. Humphrey, Historical Summary of Coal-Mine Explosions in the United States 1810-1958, Washington D.C.: United States Government Printing Office, 1960.

[34] The National Institute for Occupational Safety and Health, "All Mining Disasters: 1839 to Present," [Online]. Available: https://www.cdc.gov/niosh/mining/statistics/content/allminingdisasters.html. [Accessed 24 November 2019].

[35] United States Mine Rescue Association, "Mine Disasters in the United States," [Online]. Available: https://usminedisasters.miningquiz.com/saxsewell/black_heath.htm. [Accessed 31 January 2020].

[36] J. J. L. d. Plessis, "Active explosion barrier performance against methane and coal dust explosions," *Int J Coal Sci Technol*, vol. 2, no. 4, pp. 261-268, 2015.

[37] C. K. Man and K. A. Teacoach, "How does limestone rock dust preent coal dust explosions in coal mines?," [Online]. Available: https://www.cdc.gov/NIOSH/Mining/UserFiles/works/pdfs/hdlrdp.pdf. [Accessed 23 November 2019].

[38] H. Späth, A. S. Yu and N. Dewen, "A New Dimension in Coal Mine Safety: ExploSpot, Active Explosion Supression Technology," in *First International Symposium on Mine Safety Science and Engineering*, 2011.

[39] M. J. Brnich and K. M. Kowalski-Trakofker, "Underground Coal Mine Disasters 1900-2010: Events, Responses, and a Look to the Future," [Online]. Available: https://www.cdc.gov/niosh/mining/userfiles/works/pdfs/ucmdn.pdf. [Accessed 3 February 2020].

[40] West Virginia Office of Miners, "5.4 Flames and Forces," [Online]. Available: https://minesafety.wv.gov/PDFs/sago/Sagoreport/for%20web%201-20-07/Sago%20Report_by%20Section/Section%205_The%20Investigation_part%204.pdf. [Accessed 3 February 2020].

[41] J. F. Brune, "Methane-air explosion hazard within coal mine gobs," *Transactions of the Society for Mining, Metallurgy, and Exploration*, vol. 334, pp. 376-390, 2013.

[42] H. Editors, "Three people killed, hundreds injured in Boston Marathon bombing," HISTORY, 27 July 2019. [Online]. Available: https://www.history.com/this-day-in-history/three-people-killed-hundreds-injured-in-boston-marathon-bombing. [Accessed 29 January 2020].

[43] C. Whitlock, "Homemade, Cheap and Dangerous," Washington Post Foreign Service, 5 July 2007. [Online]. Available: https://www.washingtonpost.com/wp-dyn/content/article/2007/07/04/AR2007070401814_pf.html. [Accessed 29 January 2020].

[44] D. H. Lou Michel, in *American Terrorist: Timothy McVeigh & the Oklahoma City Bombing*, New York: Regan Books, 2001, p. 164.

[45] S. Shariat, S. Mallonee and S. S. Stidham, "Oklahoma City Bombing Injuries," December 1998. [Online]. Available: https://www.ok.gov/health2/documents/OKC_Bombing.pdf. [Accessed 29 January 2020].

[46] S. Horton, "Structural Damage: Downtown Oklahoma City," NewsOK.com, 2005. [Online]. Available: https://bombing.newsok.com/bombing/map/. [Accessed 29 January 2020].

[47] Ada Derana, "Death toll from Easter Sunday attacks climbs to 321," 23 April 2019. [Online]. Available: http://www.adaderana.lk/news/54578/death-toll-from-easter-sunday-attacks-climbs-to-321. [Accessed 29 January 2020].

[48] The Straits Times, "'Mother of Satan' bombs show foreign hand in Sri Lanka bombings: Investigtors," 21 May 2019. [Online]. Available: https://www.straitstimes.com/asia/south-asia/mother-of-satan-bombs-show-foreign-hand-in-sri-lanka-bombings-investigators. [Accessed 29 January 2020].

[49] A-P-T Research Inc., "IMESAFR," [Online]. Available: https://www.apt-research.com/products/imesafr/. [Accessed 30 January 2020].

[50] Institute of Makers of Explosives, "IMESAFR," [Online]. Available: https://www.ime.org/content/imesafr_learn_more. [Accessed 30 January 2020].

[51] Z. Koccaz, F. Sutcu and N. Torunbalci, "Architectural and Structural Design for Blast Resistant Buildings," in *The 14th World Conference on Earthquake Engineering*, Beijing, 2008.

[52] I. G. Bowen, E. R. Fletcher and D. R. Richmond, "Estimate of Man's Tolerance to the Direct Effects of Air Blast," October 1968. [Online]. Available: https://pdfs.semanticscholar.org/846a/261b91b315c329c2ab507572b40bbfee4de6.pdf?_ga=2.14215348.286177020.1580409196-1518186428.1580409196. [Accessed 30 January 2020].

[53] M. W. Courtney and A. C. Courtney, "Working toward exposure thresholds for blast-induced traumatic brain injury: Thoracic and acceleration mechanisms," 17 May 2010. [Online]. Available: https://reader.elsevier.com/reader/sd/pii/S1053811910007573?token=029DDD26C3B990871871C10A249C2F98921B96EA336A4BDD8D84ADA839FA7A13674540C10DB5866B3E293E393634037A. [Accessed 30 January 2020].

[54] R. G. DePalma, D. G. Burris, H. R. Champion and M. J. Hodgson, "Blast Injuries," *The New England Journal of Medicine,* no. 325, pp. 1335-1342, 2005.

[55] B. Rutter, "Pressure versus impulse graph for blast-induced traumatic brain injury and correlation to observable blast injuries," 2019. [Online]. Available: https://scholarsmine.mst.edu/cgi/viewcontent.cgi?article=3796&context=doctoral_dissertations. [Accessed 25 November 2019].

[56] A. Hernandez, C. Tan, F. Plattner, A. F. Logsdon, K. Pozo, M. A. Yousuf, T. Singh, R. C. Turner, P. B. Like-Wold, J. D. Huber, C. L. Rosen and J. A. Bibb, "Exposure to mild blast forces induces neuropathological effects, neurophysiological deficits and biochemical changes," *Molecular Brain,* no. 11, p. 64, 2018.

[57] L. M. Konan, H. Song, G. Pentecost, D. Fogwe, T. Ndam, J. Cui, C. E. Johnson, D. Grant, T. White, M. Chen, W. Xia, I. Cernak, R. G. DePalma and Z. Gu, "Multi-Focal Neuronal Ultrastructural Abnormalities and Synaptic Alterations in Mice after Low-Intensity Blast Exposure," *Journal of Neurotrauma,* vol. 36, no. 13, pp. 2117-2128, 2019.

[58] W. Carr, J. R. Stone, T. Walilko, L. A. Young, T. L. Snook, M. E. Paggi, J. W. Tsao, C. J. Jankosky, R. V. Parish and S. T. Ahlers, "Repeated Low-Level Blast Exposure: A Descriptive Human Subjects Study," *Military Medicine,* vol. 181, no. 5, p. 28, 2016.

[59] Rand Corporation, "The Neurological Effects of Repeated Exposure to Military Occupational Blasts," 12-14 March 2018. [Online]. Available: https://www.rand.org/content/dam/rand/pubs/conf_proceedings/CF300/CF380z1/RAND_CF380z1.pdf. [Accessed 30 January 2020].

[60] T. Shanker and R. A. J. Oppel, "War's Elite Tought Guys, Hesitant to Seek Healing," New York Times, 5 June 2014. [Online]. Available: https://www.nytimes.com/2014/06/06/us/politics/wars-elite-tough-guys-hesitant-to-seek-healing.html. [Accessed 30 January 2020].

[61] S. C. Garcia, "Marines," 3 January 2017. [Online]. Available: https://www.marines.mil/Photos/?igphoto=2001683567. [Accessed 30 January 2020].

[62] D. C. Weggel, "Blast threats and blast loading," in *Blast Protection of Civil Infrastructures and Vehicles Using Composites*, Woodhead Publishing, 2010, pp. 3-43.

[63] Alford, "Gatecrasher," 2014. [Online]. Available: https://explosives.net/gatecrasher/. [Accessed 10 2 2020].

[64] Federation of American Scientists Military Analysis Network, "M112 Composition C4 Block Demolition Charge," 12 9 1998. [Online]. Available: https://fas.org/man/dod-101/sys/land/m112-c4.htm. [Accessed 10 2 2020].

[65] "Model: 102B04," PCB Piezotronics, [Online]. Available: https://www.pcb.com/products?m=102b04. [Accessed 22 November 2019].

[66] "v2012," Phantom, [Online]. Available: https://www.phantomhighspeed.com/products/cameras/ultrahighspeed/v2012. [Accessed 22 November 2019].

[67] "Synergy P," Hi-Techniques, [Online]. Available: https://www.hi-techniques.com/products/synergy/p.html.

[68] Austin Powder Company, "RockStar Detonators," 7 March 2017. [Online]. Available: https://www.austinpowder.com/wp-content/themes/AustinPowder/documents/unitedstates/Rock_Star.pdf. [Accessed 7 November 2019].

[69] Austin Powder Company, "Electric & Electronic Detonators Safety Data Sheet," 24 January 2019. [Online]. Available: https://www.austinpowder.com/wp-content/themes/AustinPowder/documents/unitedstates/SDS-P-9-Electric-and-Electronic-Detonators-AP.pdf. [Accessed 7 November 2019].

[70] A. S. Dukhin and P. J. Goetz, "Characterization of Liquids, Nano- and Microparticulates, and Porous Bodies Using Ultrasound," *Studies in Interface Science*, vol. 24, pp. 91-125, 2010.

[71] P. Regtien and E. Dertien, "Acoustic Sensors," in *Sensors for Mechatronics (Second Edition)*, Elsevier Inc., 2018, pp. 267-303.

# VITA

David Pierre Doucet graduated from Monsignor Kelly Catholic High School in Beaumont, Texas in May of 2013. He received his Bachelor of Science degree in Chemical Engineering from Rice University in May of 2017. He earned his Master of Science in Explosives Engineering from the Missouri University of Science and Technology in May of 2020.